Validation of IASI satellite ammonia observations at the pixel scale using in-situ vertical profiles

Xuehui Guo[1], Lieven Clarisse[2], Rui Wang[1], Martin Van Damme[2], Simon Whitburn[2], Pierre-François Coheur[2], Cathy Clerbaux[2,3], Bruno Franco[2], Da Pan[1], Levi M. Golston[1,4†], Lars Wendt[1,5], Kang Sun[1,6†], Lei Tao[1,7], David Miller[1,8†], Tomas Mikoviny[9,10,11†], Markus Müller[12,13†], Armin Wisthaler[12,11], Alexandra G. Tevlin[14,15†], Jennifer G. Murphy[14], John B. Nowak[16,17†], Joseph R. Roscioli[16], Rainer Volkamer[18,19,20], Natalie Kille[18,19,20], J. Andrew Neuman[19,21], Scott J. Eilerman[22], James H. Crawford[17], Tara I. Yacovitch[16], John D. Barrick[17], Amy Jo Scarino[17], and Mark A. Zondlo[1*]

[1]Department of Civil and Environmental Engineering, Princeton University, Princeton, NJ, USA

[2]Université libre de Bruxelles (ULB), Spectroscopy, Quantum Chemistry and Atmospheric Remote Sensing (SQUARES), Brussels, Belgium

[3]LATMOS/IPSL, Sorbonne Université, UVSQ, CNRS, Paris, France

[4]Atmospheric Science Branch, NASA Ames Research Center, Moffett Field, CA, USA

[5]Hunterdon Central Regional High School, Flemington, NJ, USA

[6]Department of Civil, Structural and Environmental Engineering, University at Buffalo, Buffalo, NY, USA

[7]Princeton Institute for the Science and Technology of Materials, Princeton, NJ, USA

[8]Sonoma Technology, Inc., Washington, D.C., USA

[9]Chemistry and Dynamics Branch, Science Directorate, NASA Langley Research Center, Hampton, VA, USA

[10]Oak Ridge Associated Universities, Oak Ridge, TN, USA

[11]Department of Chemistry, University of Oslo, Oslo, Norway

[12]Institute for Ion Physics and Applied Physics, University of Innsbruck, Innsbruck, Austria

[13]Ionicon Analytik, Innsbruck, Austria

[14]Department of Chemistry, University of Toronto, Toronto, Ontario, Canada

[15]Environment and Climate Change Canada, Toronto, ON, Canada

[16]Aerodyne Research Inc., Billerica, MA, USA

[17]NASA Langley Research Center, Hampton, VA, USA

[18]Department of Chemistry, University of Colorado Boulder, Boulder, CO, USA

[19]Cooperative Institute for Research in Environmental Sciences (CIRES), University of Colorado Boulder, Boulder, CO, USA

[20]Department of Atmospheric Sciences, University of Colorado Boulder, Boulder, CO, USA

[21]NOAA Chemical Sciences Laboratory (CSL), Boulder, CO, USA

[22]Jupiter Intelligence, Boulder, Colorado 80302, USA

† - current affiliation

*Corresponding author: Mark A. Zondlo (mzondlo@princeton.edu)

Key Points:

- IASI NH_3 columns agree well with those derived from boundary layer, in-situ measurements with no significant biases at the pixel scale
- Validation in a hotspot region shows best agreement at narrow spatiotemporal scales on the order of the pixel size and mean transport time
- Additional accurate, airborne-based NH_3 datasets are critically needed for improved validations across a range of environments

Abstract

Satellite ammonia (NH_3) observations provide unprecedented insights into NH_3 emissions, spatiotemporal variabilities and trends, but validation with in-situ measurements remains lacking. Here, total columns from the Infrared Atmospheric Sounding Interferometer (IASI) were intercompared to boundary layer NH_3 profiles derived from aircraft- and surface-based measurements primarily in Colorado, USA, in the summer of 2014. IASI-NH_3 version 3 near real-time dataset compared well to in-situ derived columns (windows ±15 km around centroid, ±1 hour around overpass time) with a correlation of 0.58, a slope of 0.78±0.14, and an intercept of $2.1\times10^{15}\pm1.5\times10^{15}$ molecules cm^{-2}. Agreement degrades at larger spatiotemporal windows, consistent with the short atmospheric lifetime of NH_3. We also examined IASI version 3R data, which relies on temperature retrievals from the ERA Reanalysis, and a third product generated using aircraft-measured temperature profiles. The overall agreement improves slightly for both cases, and neither is biased within their combined measurement errors. Thus, spatiotemporal averaging of IASI over large windows can be used to reduce retrieval noise. Nonetheless, sampling artifacts of airborne NH_3 instruments result in significant uncertainties of the in-situ-derived columns. For example, large validation differences exist between ascent and descent profiles, and the assumptions of the free tropospheric NH_3 profiles used above the aircraft ceiling significantly impact the validation. Because short-lived species like NH_3 largely reside within the boundary layer with complex vertical structures, more comprehensive validation is needed across a wide range of environments. More accurate and widespread in-situ NH_3 datasets are therefore required for improved validations of satellite products.

Plain Language Summary

Ammonia is an important species in the atmosphere that contributes to $PM_{2.5}$ formation, but it is challenging to measure. The major source of ammonia is agricultural activities. Improving our estimate of ammonia emissions requires widespread and frequent measurements such as those from satellite. To date, satellite-based ammonia measurements have not been extensively validated, particularly on the scale of individual measurements. We have compared satellite ammonia measurements with those from ground-based and aircraft measurements and show that

satellite measurements are accurate at the scale of an individual pixel. However, we also show that it is important to consider the spatial and temporal differences between the measurement scales (satellite vs. ground- and aircraft-based) in regions where ammonia is concentrated, and large sources exist. Improved validations will require advances in airborne ammonia measurement technologies, particularly for the relatively low levels of ammonia that exist above the boundary layer or away from strong sources. Finally, additional airborne-based measurements are needed to compare to satellite-based measurements in other regions and seasons to extend these conclusions to a global scale.

1. Introduction

Gas-phase ammonia (NH_3) is a ubiquitous base in the atmosphere and an important component of the nitrogen cycle. Atmospheric NH_3 reacts with sulfuric acid and nitric acid to form ammoniated (NH_4^+) aerosol particles, reducing visibility and causing adverse effects on human health (Mensink & Deutsch, 2008; Ostro *et al.*, 2015; Wang *et al.*, 2006). Ammoniated aerosols also affect the climate by scattering solar radiation, resulting in a negative radiative forcing (IPCC, 2013). Excess NH_3 deposited to ecosystems can cause soil acidification, water eutrophication and loss of biodiversity (Galloway *et al.*, 2004). Research suggests that NH_3 and NH_4^+ have become important contributors to the dry and wet deposition of reactive nitrogen (N_r) in most regions of the United States due to reductions in nitrogen oxides (NO_x) emissions (Li *et al.*, 2016).

Agricultural activities such as fertilizer application and livestock waste management contribute to over 80% of total NH_3 emissions globally (Bouwman *et al.*, 1997; Paulot *et al.*, 2014). Other anthropogenic sources of NH_3 include chemical production, residential waste and vehicle emissions (Behera *et al.*, 2013; Sun *et al.*, 2017; Van Damme *et al.*, 2018). Global NH_3 emissions are expected to increase in the forthcoming decades due to growing food demands (Erisman *et al.*, 2008; Lamarque *et al.*, 2011). NH_3 is unregulated in many countries, but active efforts are being made to quantify NH_3 emissions and understand their trends on regional to global scales (Paulot *et al.*, 2014; Van Damme *et al.*, 2018). There remain significant uncertainties in bottom-up NH_3 emission inventories as they require representative measurements to scale from a small subset of sources to the entire global budget (Beusen *et al.*, 2008; Golston *et al.*, 2020; Zhang *et al.*, 2018). On the other hand, top-down approaches that depend on inverse modeling of NH_4^+ wet deposition data require widespread observations, accurate vertical profiles, and estimates of chemical and deposition lifetimes (Paulot *et al.*, 2014; Zhu *et al.*, 2013). However, current major monitoring networks such as the Ammonia Monitoring Network (AMoN) in the U.S. and the Nationwide Nitrogen Deposition Monitoring Network (NNDMN) in China lack the spatial coverage and temporal resolution needed to fully resolve the variabilities of NH_3, thereby introducing uncertainties in top-down estimates of NH_3 emissions (National Atmospheric Deposition Program, 2019; Xu *et al.*, 2015).

In the past decade, advances in remote sensing techniques have provided unprecedented global coverage and medium-term time series for studying NH_3 on a broader scale than achievable by ground-based measurements. Since the early 2000s, several satellites have been launched into space with infrared sounders to measure atmospheric constituents. Examples of satellites instruments that can measure NH_3 are the Tropospheric Emission Spectrometer (TES) (Shephard *et al.*, 2011), Infrared Atmospheric Sounding Interferometer (IASI) (Clarisse *et al.*,

2009; Van Damme *et al.*, 2017; Whitburn *et al.*, 2016), Cross-track Infrared Sounder (CrIS) (Shephard & Cady-Pereira, 2015), Atmospheric Infrared Sounder (AIRS) (Warner *et al.*, 2016) and Greenhouse Gases Observing Satellite (GOSAT) (Someya, Imasu, Shiomi, & Saitoh, 2020). Launched in 2004 and having ended its mission in 2018, TES provided the first satellite-based NH_3 product, though it only performed limited measurements in its later years (Rasmussen, 2018). IASI provides Level-2 (L2) NH_3 products dating back to 2008 with much broader spatial coverage than TES. AIRS has the longest data record of NH_3 on a single satellite between 2002 and 2016 (Warner *et al.*, 2017). CrIS and GOSAT have also provided NH_3 products, but with limited availability at this time (Dammers *et al.*, 2019; Someya *et al.*, 2020).

Despite the increasing use of satellite NH_3 products for inventory assessments, nitrogen deposition, and aerosol chemistry, validation of satellite NH_3 measurements, especially against independent in-situ measurements, remains limited (Dammers *et al.*, 2019; Van Damme *et al.*, 2018; Zhang *et al.*, 2018). Although satellite data averaged over a large domain or an extended period can be used to study regional and global characteristics of NH_3, validations of individual satellite pixels help further understand the capabilities and limitations of satellite observations. Meanwhile, analyses of satellite NH_3 on fine temporal (e.g. daily and weekly) and local scales, such as studying fertilizer emissions, require validation for increased confidence (Fortems-Cheiney *et al.*, 2016; Van Damme *et al.*, 2018). Previously, Van Damme *et al.* (2015a) used an averaged GEOS-Chem model profile to convert IASI NH_3 columns into surface concentrations and found fair agreements between IASI and ground-based observations on monthly scales, and moderate correlations with hourly airborne data, but the fixed profile shapes used for the conversion introduced certain biases in IASI surface concentration estimations. Dammers *et al.* (2016) validated IASI using column measurements from ground-based high-resolution Fourier-transform infrared spectroscopy (FTIR) at nine locations worldwide with spatial and temporal windows of 25 km and 90 min, respectively. Correlations of ~0.8 were found where NH_3 levels were high, though the study removed outliers during wintertime. In addition, the FTIR measurements themselves have not been validated by in-situ profiles and instead rely upon model a priori and limited surface observations (Dammers *et al.*, 2015). Similarly, a comparison between CrIS and FTIR was conducted by Dammers *et al.* (2017), where an overall correlation of 0.8 was observed, but the agreements for individual sites varied largely. Using a different method, Sun *et al.* (2015) conducted a validation of TES NH_3 with collocated aircraft and mobile lab measurements in California at the pixel scale and found the agreement to be within 10% for selected dates. Furthermore, the spatial variability of NH_3 columns within a satellite pixel (IASI: ~ 12 km in diameter) has been assessed over Colorado using structure functions analyses (Follette-Cook *et al.*, 2015) of mobile NH_3 column observations conducted on fine spatial scales (few tens of meters; Kille *et al.*, 2017). During the time of the study, 50% of the variability in NH_3 columns was found within approximately 1.6 km, and 90% of the variability within 6 km (Kille *et al.*, 2017). The high variability of atmospheric NH_3 poses a fundamental sampling challenge to satellite validation on the pixel scale and illustrates the need for a multi-platform sampling strategy for best results.

To expand the scope and robustness of satellite NH_3 validations, we compare the IASI NH_3 at the pixel scale with a combination of aircraft-based profiles and an assortment of other in-situ fixed and mobile column surface observations taken during the summer of 2014 in Colorado, USA, and provide some insights on the winter of 2013 in California, USA. The general approach used here can be readily applied to other satellite NH_3 products, provided that

165 NH_3 vertical profiles are collocated with the satellite pixels within a temporal window that is
166 consistent with wind and atmospheric transport.

2. Data and Methods

2.1. IASI Observations

IASI is an infrared sounder onboard the polar-orbiting MetOp-A/B/C satellites, which were respectively launched in 2006, 2012 and 2018 (Clerbaux *et al.*, 2009). It is sensitive to NH_3 absorption features mainly between 800 and 1200 cm^{-1} (Clarisse *et al.*, 2010; Coheur *et al.*, 2009). IASI provides twice-daily measurements of NH_3 with overpass times of 0930/2130 local solar time (LST). IASI has a swath of 2400 km and a pixel size of 12 km in diameter at nadir. The first IASI NH_3 product was retrieved using lookup tables (LUTs) based on simulations from a forward radiative transfer model. A hyperspectral range index (HRI) was calculated from each observation and converted to NH_3 columns using the LUTs (Van Damme *et al.*, 2014). A subsequent version (ANNI-NH3-v1) improved the retrieval of NH_3 by using an artificial neural network for IASI (ANNI) to transform the calculated HRI into column densities (Whitburn *et al.*, 2016). Version 2 of the ANNI product further improved the algorithm by introducing separate neural networks for land and sea scenes, and simplified input parameters. With the release of this version, an additional product was made available using meteorological inputs from the European Centre for Medium-Range Weather Forecasts (ECMWF) Re-Analysis (ERA)-Interim dataset for better interannual consistency, as opposed to using meteorological retrievals from IASI itself to calculate columns (Van Damme *et al.*, 2017).

In this work, we analyze version 3 of the ANNI-NH_3 product from IASI MetOp-A/B. This version, processed using the retrieval framework outlined in Franco *et al.* (2018), features a slightly increased measurement sensitivity due to small changes in the neural network architecture and training and improved post-filtering. In addition, several debiasing procedures have been introduced to correct for the gradual increase of CO_2 columns over the entire IASI time-period and for IASI instrument calibrations. Despite the significant number of changes from version 2 to version 3, the changes to the retrieved columns are modest in the mean. For columns above 4×10^{15} molecules cm^{-2}, 80% of the data agree to within 20%. As infrared retrievals are known to be quite sensitive to auxiliary input data, we evaluate the following products: (1) The near real-time product, retrieved using meteorological data from the European Organisation for the Exploitation of Meteorological Satellites (EUMETSAT) with cloud coverage < 25%, (2) the reanalysis product, retrieved using meteorological data from ERA5/ECMWF with cloud coverage < 10%, and (3) a dedicated product retrieved using collocated in-situ temperature profiles from aircraft, sonde and mobile measurements (other meteorological data such as skin temperature are from EUMETSAT) with cloud coverage < 25%. The cloud coverage flag in the reanalysis product is stricter (10%) than the near real-time product in order to provide a higher quality dataset (e.g. for long-term trends), whereas the near real-time product defaults to 25% (see Van Damme *et al.*, 2017). While nighttime observations also offer the possibility to measure NH_3 (e.g. Van Damme, *et al.*, 2015b), we only include the morning observations over land surfaces as IASI has better sensitivity to NH_3 under these conditions. In addition, there were no aircraft profiles available near the nighttime IASI overpass time (~2130 LST).

We note that the ANNI-NH3 products do not generate averaging kernels (AVKs) because the current retrieval method is not based on optimal estimation (i.e. the retrieval is unconstrained). We refer to Whitburn *et al.* (2016) and Van Damme *et al.* (2017) for a comprehensive discussion on the advantages and disadvantage of the neural network retrieval

approach for NH_3. In short, one advantage of the current approach is that the reported NH_3 column values are directly comparable to models and observations as the retrieval includes an assumption about the NH_3 vertical distribution. The product does not exhibit biases over areas where the sensitivity is low (and for which an optimal estimation retrieval would return a value close to its a priori). The disadvantage is that the uncertainty in the measurements can be very large. As a compromise, the retrieval employs a post-filter that removes those measurements where the information content is close to zero. The upshot is that the measurements that pass the post-filter are meant to be used at face value, together with the derived uncertainty; and it is in this way that we perform the validation here. This also reflects how the users typically work with the product. Evaluating the sensitivity of thermal infrared sounders to the boundary layer is both out of the scope of this work and largely duplicates with previous studies (Bauduin, *et al.*, 2014; Clarisse *et al.*, 2010; Whitburn *et al.*, 2016). Thus, only the unconstrained columns were used to provide an overview of the agreement between IASI and in-situ measurements.

2.2. In-situ Measurements

The Deriving Information on Surface conditions from Column and Vertically Resolved Observations Relevant to Air Quality (DISCOVER-AQ) field experiment was a multi-year campaign led by the National Aeronautics and Space Administration (NASA) (Crawford & Pickering, 2014). Its mission was to validate collocated satellite observations of atmospheric pollutants over four regions in the U.S. (Baltimore/Washington, California, Houston, and Colorado). Airborne NH_3 measurements were only available in the California and Colorado campaigns. The California campaign occurred between January 16 and February 7, 2013 over the San Joaquin Valley. In the following year, the experiment was continued in Colorado from July 16 to August 16, along with a complimentary National Science Foundation (NSF) Front Range Air Pollution and Photochemistry Experiment (FRAPPÉ) that had additional platforms and NH_3 measurements (Flocke *et al.*, 2020). The DISCOVER-AQ flight patterns were specifically designed for satellite validations as the P-3B aircraft made repeated upward and downward spirals. Vertical profiles were performed at designated locations where there were collocated ground monitoring sites managed by the Colorado Department of Public Health and Environment and the National Oceanic and Atmospheric Administration (NOAA). A typical P-3B spiral roughly spanned 5 km in diameter, which is particularly advantageous for validations of short-lived species such as NH_3 that exhibit strong spatial gradients near source regions.

A unique aspect of the 2014 Colorado campaign compared to past field experiments was the comprehensive suite of NH_3 measurements on multiple platforms: two aircraft, a tall tower, and four mobile laboratories. The NASA P-3B aircraft measured NH_3 with a proton-transfer time-of-flight mass spectrometer (PTR-MS) (Müller *et al.*, 2014). It is emphasized that NH_3 data were only a side product of the PTR-MS measurements during DISCOVER-AQ. The instrument was primarily measuring volatile organic compounds (VOCs) and thus not optimized for detecting NH_3 (i.e. a high instrumental background resulting in a worse detection limit and slower time response due to a ~2 m long inlet line, compared to an optimized NH_3 measurement). The NSF/NCAR C-130 aircraft measured NH_3 with a closed-path, quantum cascade laser-based instrument using a fast-response inertial inlet to minimize sampling artifacts (QC-TILDAS, Aerodyne Research Inc.) (Schiferl *et al.*, 2016). A moving carriage on the Boulder Atmospheric Observatory's (BAO) 300 m tall tower in Erie, Colorado made profiles every hour and was equipped with a closed-path, quantum cascade laser-based NH_3 instrument

(QC-TILDAS, Aerodyne Research Inc.) (Tevlin *et al.*, 2017). The mobile laboratories included in-situ measurements from an open-path, quantum cascade laser-based instrument onboard the Princeton Atmospheric Chemistry Experiment, a cavity ring down instrument (Picarro G2103) onboard the NOAA Chemical Sciences Division (CSD) van, and a closed-path, quantum cascade laser-based instrument (QC-TILDAS) on the Aerodyne Mobile Laboratory (Eilerman *et al.*, 2016; Herndon *et al.*, 2005; Tao *et al.*, 2015). These three mobile laboratories conducted stationary and moving intercomparisons and showed agreement to within 10% on average (Golston *et al.*, 2020). Column NH_3 abundances were measured by the University of Colorado Solar Occultation Flux (CU SOF) instrument onboard the CU/NCAR mobile laboratory (Kille *et al.*, 2017). CU SOF couples a digital fast solar tracker (Baidar *et al.*, 2016; Patent No. 10379194, 2019) to a fast scanning FTIR to measure the vertical column integral of NH_3 and other gases above the mobile platform directly in the open atmosphere (Kille *et al.*, 2017). Table 1 summarizes the performances of the NH_3 instruments during the California and Colorado campaigns.

In addition to the NH_3 measurements, temperature and pressure measurements were taken from the P-3B aircraft and specially launched radiosondes (iMet-1 & Vaisala RS92) timed with aircraft flights. These data allowed for the construction of in-situ derived NH_3 columns and for the generation of the third IASI NH_3 product with in-situ temperature measurements as input. For the determination of atmospheric mixed layer height (MLH) used in the construction of in-situ NH_3 profiles, we examined P-3B aircraft profiles of other short-lived species with sources in this region including nitrogen dioxide (NO_2) (Weinheimer *et al.*, 1994), ethane (C_2H_6) from gas-oil activities (Yacovitch *et al.*, 2014), and the number concentration of particles (CN) with diameters > 10 nm from the LARGE instrument (Beyersdorf *et al.*, 2016). Additional MLH measurements were incorporated from the High Spectral Resolution LIDAR 2 (HSRL2) instrument onboard the NASA B200 aircraft (Scarino *et al.*, 2014). Table 2 lists the dates on which each platform measuring NH_3 was operational during these campaigns.

Table 1. *Summary of in-situ NH_3 measurements during DISCOVER-AQ*

Platform	Method	Typical uncertainty	Referenced Work
California (2013)			
NASA P-3B aircraft	PTR-MS	± 35%	(Müller *et al.*, 2014)
NASA P-3B aircraft	CRDS	± (35% + 1.7 ppbv) + 0.2 ppbv[a]	(Schiferl *et al.*, 2016)
Princeton mobile	Open-path QCL	± 20%	(Miller *et al.*, 2015)
Colorado (2014)			
NASA P-3B aircraft	PTR-MS	± 35%	(Müller *et al.*, 2014)
NSF/NCAR C-130 aircraft	QC-TILDAS	± (22% + 0.305 ppbv) + 0.058 ppbv [a]	(Ellis *et al.*, 2010; Schiferl *et al.*, 2016)
Aerodyne mobile	QC-TILDAS	± (22% + 0.305 ppbv) + 0.058 ppbv [a]	(Ellis *et al.*, 2010; Schiferl *et al.*, 2016)
Princeton mobile	Open-path QCL	± 10% + 0.2 ppbv [a]	(Miller *et al.*, 2014; Tao *et al.*, 2015)

CU/NCAR mobile	SOF	± 4.4% + 1×10^{15} molecules cm^{-2} [a]	(Kille *et al.*, 2017)
NOAA CSD mobile	CRDS	± 20% + 1 ppbv [a]	(Eilerman *et al.*, 2016)
NOAA BAO tower	QC-TILDAS	± 20% + 0.5 ppbv [a]	(Tevlin *et al.*, 2017)

Note. PTR-MS = proton transfer reaction-mass spectrometer; CRDS = cavity ring down spectrometer; QCL = quantum cascade laser; NSF = National Science Foundation; NCAR = National Center for Atmospheric Research; QC-TILDAS = quantum cascade tunable infrared laser direct/differential absorption spectroscopy; CU = University of Colorado; SOF = Solar Occultation Flux. BAO = Boulder Atmospheric Observatory. Uncertainties are presented as reported in archived field data catalog and/or related publications. Subscripts in the third column: [a] total uncertainty + limit of detection. In some cases, total uncertainty is reported as a combination of a relative amount plus an absolute amount (% + X ppbv).

Table 2. *Availability of in-situ NH_3 measurements in DISCOVER-AQ California in 2013 (upper table) and Colorado in 2014 (lower table). Colored and blank cells represent dates when data from each platform were or were not available, respectively.*

Platform \ Date	1/16	1/17	1/18	1/19	1/20	1/21	1/22	1/25	1/26	1/27	1/28	1/29	1/30	1/31	2/1	2/3	2/4	2/5	2/6	2/7
NASA P-3B (PTR-MS, A.Wisthaler)																				
NASA P-3B (CRDS, J. Nowak & A. Neuman)																				
Princeton mobile (Open-path QCL, M. Zondlo)																				

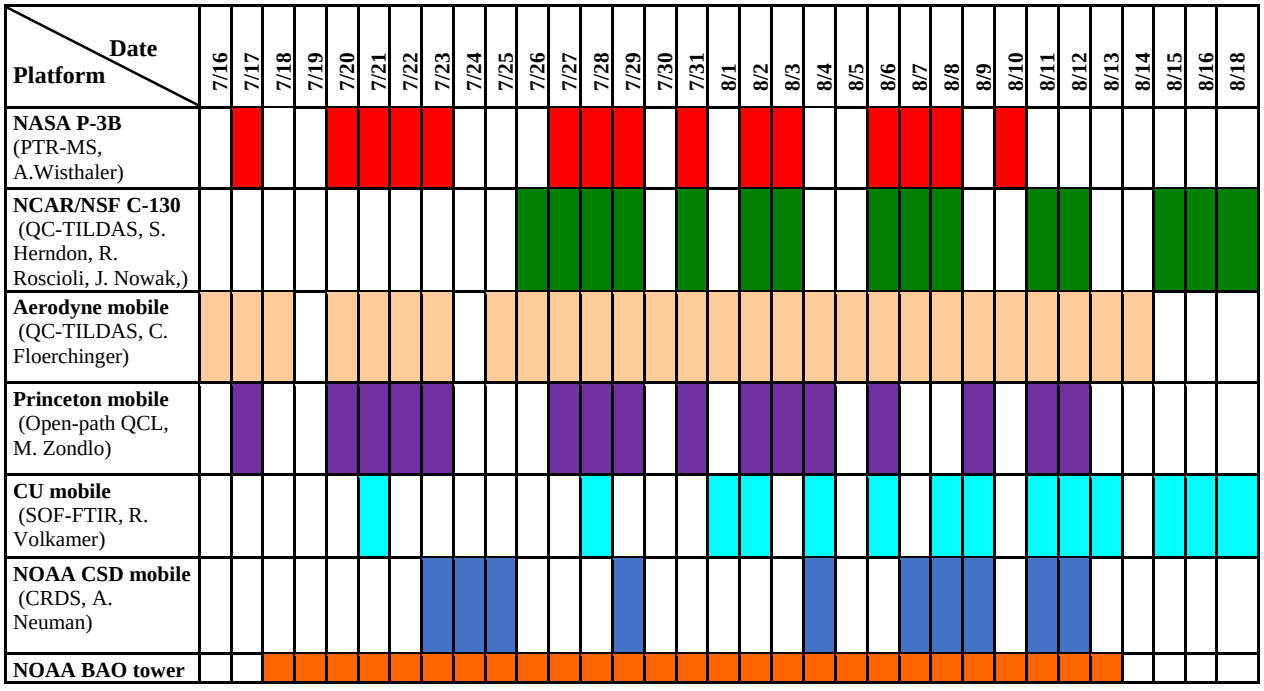

(QC-TILDAS, J. Murphy)	

2.3. Validation Algorithm

2.3.1. Spatiotemporal filtering

The general framework of the validation algorithm used in this study is shown in Figure 1. For each valid IASI observation, we applied a spatiotemporal window centered on the pixel's center location and overpass time to filter for DISCOVER-AQ data within the designated window. For example, if an in-situ measurement was made within a certain spatial distance (e.g. ±15 km) from the center of the IASI pixel, and the time difference relative to the IASI overpass time was within the temporal window (e.g. ±1 hour), the measurement was considered valid for comparison. This applied to all in-situ NH_3 measurements and other relevant data (e.g. B200). One exception was the radiosondes, where we used the most temporally relevant launch even if the instrument was located outside the window, especially when using smaller spatial windows. The other exception was the P-3B aircraft profiles, where all the data were included in a vertical profile if the geographical center (mean latitude and longitude) of the aircraft spiral fell inside the spatial window but parts of the spiral itself were outside the window.

We determined the optimal size of the spatiotemporal window based on wind speeds in the boundary layer. To calculate typical boundary layer wind speeds, we used wind data measured at 300 m on the BAO tower located in Erie, CO (40.050° N, 105.004° W) from 0600-1200 local time during DISCOVER-AQ to bracket the IASI morning overpass times. Next, in-situ NH_3 measurements located within the spatiotemporal window were aggregated into one dataset. Each collocation between IASI and in-situ measurements required at least one aircraft profile available so that an NH_3 vertical profile could be constructed. Figure 2 shows an example of collocation between IASI and in-situ measurements on July 27, 2014. The location of the IASI pixel centroid, denoted as a "+", is positioned in the center with its footprint boundary outlined as a solid white ellipse. The spatial window (in this case, ±15 km) is plotted as a dotted white circle. For demonstration purposes only, the ±3 hour temporal window is chosen in this case to show as many different types of in-situ measurements as possible, but the vast majority of this study focuses on a ±1 hour temporal window as will be discussed later. The route of each in-situ platform is marked with a different color. In this example, in-situ NH_3 measurements were available from P-3B, C-130, Princeton mobile lab and BAO tower.

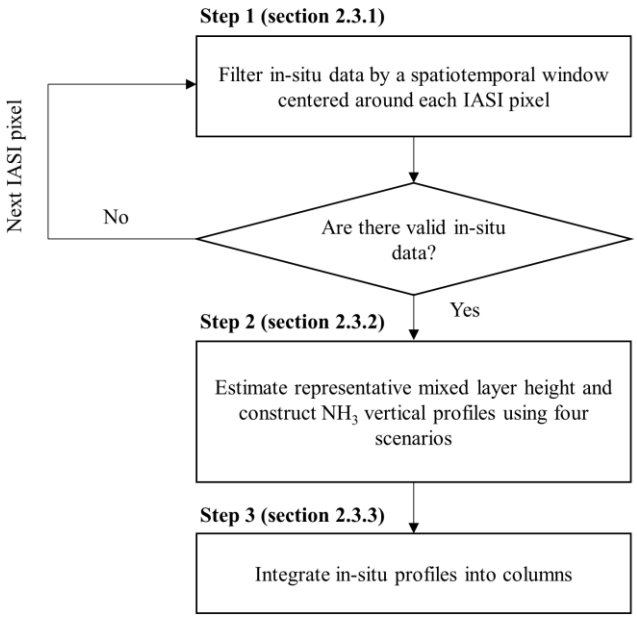

Figure 1. Overview of the validation algorithm. The flowchart is repeated for each valid IASI pixel. If no in-situ data are found within the spatiotemporal window, the pixel will be skipped, and the next available pixel will be scanned for collocation. The four scenarios in Step 2 are described in section 2.3.2 and illustrated with an example in Figure 3. Step 3 is discussed in section 2.3.3.

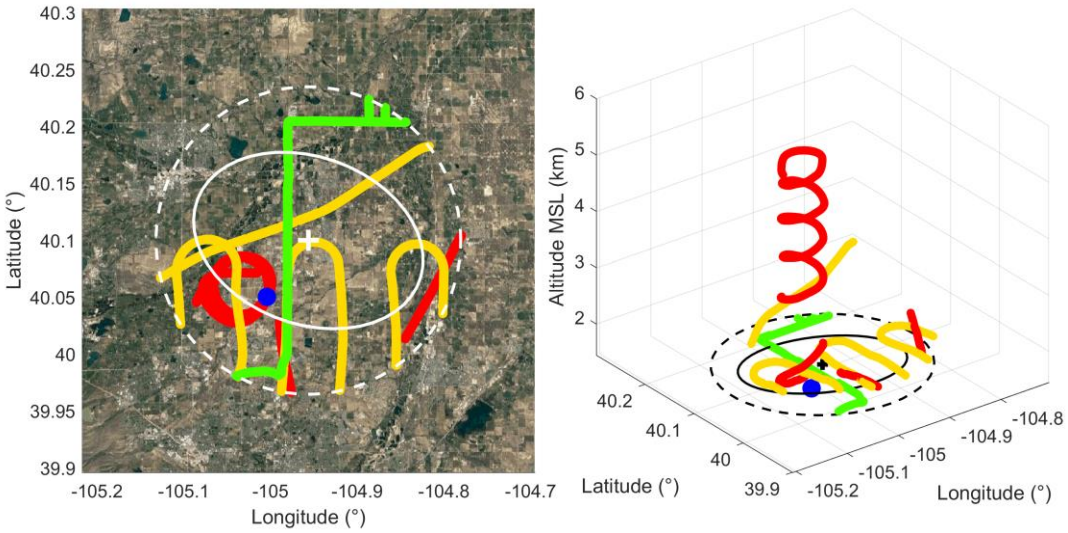

Figure 2. Example of collocated IASI and in-situ measurements on July 27, 2014 at 17:34:09 UTC. The left panel shows a two-dimensional view from the top and the right panel visualizes the movements of the in-situ platforms in a three-dimensional view. The center of the IASI pixel is denoted as "+". The solid ellipse marks the boundary of the IASI pixel. The dotted circle represents the ±15 km spatial window. Note that the ±3 hour temporal window in this case is only used to show how the choice of temporal windows impacts the availability of in-situ data.

Colored lines show the routes of the in-situ platforms: red = P-3B, yellow = C-130, green = Princeton mobile lab, blue dot = BAO tower. The 2D figure is overlaid on Google Maps (Google, Inc.) for better visualization of the geographical location and topography. Note that IASI pixels are circles of 12 km diameter at nadir, but elliptical otherwise as in this case.

2.3.2. Reconciling uncertainties in NH_3 profiles

The combined in-situ dataset was then used to calculate the integrated column density of NH_3. Two issues remained, however, in the construction of the in-situ-derived columns. First, because the aircraft ceiling on most spirals was limited to ~ 5 km above sea level, it was necessary to assume NH_3 concentrations in the middle and upper troposphere. Though NH_3 is expected to accumulate mostly in the boundary layer because of its short-lifetime on the order of hours to days (Dentener & Crutzen, 1994; Seinfeld & Pandis, 2016), NH_3 has been detected in the middle and upper troposphere previously (Whitburn *et al.*, 2016). Höpfner *et al.* (2016) for instance measured NH_3 levels in the upper troposphere to be tens of parts per trillion by volume (1 pptv = 10^{-12} mol/mol) in the outflow of an active monsoon system. However, the free tropospheric NH_3 background was below the detection limit (< 3-5 pptv). More recently, Höpfner *et al.* (2019) found that NH_3 concentrations in the upper troposphere could reach up to 1 ppbv in some regions during the Asian monsoon season, but were low in most other places. Other studies that measured NH_3 profiles showed sharp decreases of NH_3 mixing ratio over altitude (Nowak *et al.*, 2010), and low NH_3 (< 1 ppbv) at these higher altitudes (Hoell *et al.*, 1980; Ziereis & Arnold, 1986). Based on this evidence, it is reasonable to argue that NH_3 concentrations in the upper troposphere are negligible compared to the lower troposphere. Second, a problem remained on how to deal with NH_3 concentrations measured by the aircraft beyond the MLH. Previously, Sun *et al.* (2015) found that airborne NH_3 sensors (i.e. Picarro CRDS and PTR-MS on the P-3B aircraft) in DISCOVER-AQ California exhibited sampling artifacts above the MLH due to long and variable instrument response times. Because DISCOVER-AQ CA and CO were in agricultural source regions, a strong gradient existed from very high levels within the boundary layer to nominally clean free tropospheric levels. Such strong gradients can be problematic for accurately quantifying NH_3 with an instrument or inlet that has a time response slower than the rapid changes in ambient mixing ratios (Fehsenfeld *et al.*, 2002; Von Bobrutzki *et al.*, 2010).

Given these issues on the column construction from the aircraft data, we accounted for the lack of a full tropospheric profile and sampling artifacts by creating four possible scenarios that bracketed the likely NH_3 distributions above the MLH in the troposphere. Figure 3 shows a case studies used to address the vertical profile in the free troposphere: (1) integrating NH_3 only up to the MLH, assuming negligible NH_3 concentrations above. Physically, this corresponds to the assumption that NH_3 is contained within the boundary layer and dominates the column measurement based on its short lifetime. It also assumes that sampling biases of instruments are negligible in and around the strong gradient of the mixed layer. (2) Integrating NH_3 up to the maximum aircraft altitude, assuming negligible NH_3 at altitudes higher than the aircraft ceiling. This assumes that aircraft NH_3 measurements above the MLH are valid and real signals, but no extrapolation is done beyond the aircraft range. (3) Integrating NH_3 up to the tropopause with linear interpolation of decreasing mixing ratios from the maximum aircraft altitude to zero at the tropopause estimated from sonde temperature profiles. In the real atmosphere, NH_3 is removed from the atmosphere by reacting with nitric and sulfuric acids, and through dry deposition in the

gas phase and wet deposition as NH_4^+ by cloud scavenging (Mensink & Deutsch, 2008; Mizak *et al.*, 2005; Nemitz, Milford, & Sutton, 2001). The linear interpolation represents a simplistic mode of decay of NH_3 concentrations over altitude via the removal pathways. (4) Integrating NH_3 up to the tropopause, while assuming constant NH_3 mixing ratio from the maximum aircraft altitude to the tropopause. The last scenario features a well-mixed free troposphere in which NH_3 is distributed uniformly in the vertical direction. In all four scenarios, we assumed NH_3 was negligible beyond the tropopause based on previous studies (Höpfner *et al.*, 2019, 2016). These case studies of the free tropospheric NH_3 distribution helped to bracket the magnitude and importance of the full NH_3 vertical profile that was not captured by the aircraft or caused by potential sampling problems in the in-situ measurements.

Knowing the representative MLH for each collocation was necessary for the integration of NH_3 profile in the first case. We estimated the MLH using three methods to minimize potential errors and mismatches in some cases due to geographical elevation differences within the window: (1) using the altitude of the first inversion of the temperature profile from the nearest timed sonde launch (which may not necessarily be in the exact spatiotemporal window), (2) using aerosol backscatter data from the B200 aircraft within the specified spatiotemporal window, and (3) derived from the vertical profiles of other short-lived atmospheric tracers (NO_2, C_2H_6 and CN > 10 nm) measured by P-3B. The final MLH was calculated as the average of all the available methods for each collocation.

2.3.3. Vertical integration

The available in-situ NH_3 measurements at 1 Hz were vertically binned every 100 m to reduce noise, and the median value in each layer was used to build the final vertical profiles. Median values were chosen because in-situ measurements on or near the ground immediately downwind of sources (e.g. feedlots) would skew the mean to be unrepresentative of the overall layer. When there was an altitude mismatch between the lowest in-situ bin and the ground at the pixel's center location (i.e. in-situ altitude > IASI centroid altitude), the in-situ NH_3 mixing ratio was extrapolated from the lowest bin to the IASI centroid ground level. An additional requirement that there must be at least two bins between the ground and MLH was applied to reduce uncertainties due to interpolation. In cases where the IASI centroid ground altitude was higher than in-situ locations, only measurements higher than the IASI ground altitude were included. Using the ideal gas law, the column NH_3 was integrated from gas density over altitude:

$$\omega_{NH_3} = \int \frac{C_{NH_3} P_{air}}{k T_{air}} dz$$

where ω_{NH_3} is the column density of NH_3 in the same unit as IASI (molecules cm^{-2}), C_{NH_3} is the mixing ratio of NH_3 in air (ppbv), P_{air} is the air pressure (Pa), k is the Boltzmann's constant (1.38×10^{-23} J K^{-1}), T_{air} is the air temperature (K), and z is the altitude (m).

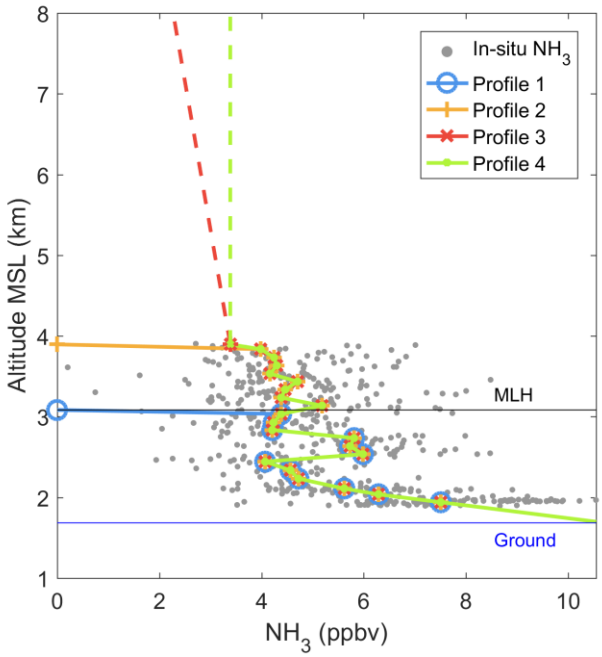

Figure 3. The four assumed NH_3 vertical profiles in this work. Profile 1 (blue): integration up to MLH with zero NH_3 above; Profile 2 (orange): integration up to maximum aircraft altitude and zero NH_3 above; Profile 3 (red): integration up to tropopause with linear interpolation of concentrations beyond aircraft altitudes to a value of zero at the tropopause; Profile 4 (green): integration up to tropopause assuming constant NH_3 beyond aircraft altitude. The median profile from each assumption is shown with the interpolated sections above the aircraft altitude plotted as dashed lines. In-situ NH_3 concentrations at 1 Hz are shown in gray. The thin blue line indicates the ground altitude at the IASI pixel center. The thin black line denotes the corresponding MLH in this case. Altitude MSL stands for altitude above mean sea level.

The in-situ temperature profiles used for generating the third alternative IASI-NH_3 product described in section 2.1 were aggregated from the in-situ platforms in section 2.2 and filtered using the spatiotemporal window of interest. Temperature measurements from radiosondes were needed to fill in the gaps of aircraft temperature measurements (e.g. near the ground, above the ceiling), yet in many cases a sonde could not be found within the window. Therefore, we always used the nearest sonde in time to construct the temperature profile, whether or not it was located within the specified spatial window. In California, however, this approach was not ideal in winter. Due to strong yet shallow inversions, there were often large discrepancies between the sonde temperatures and those measured by the aircraft, especially near the surface. To reduce errors due to spatial separation, we used P-3B aircraft temperatures where applicable and sonde measurements outside the aircraft altitude range for California. In Colorado in summer, the horizontal gradients of temperature were less pronounced, and temperature profiles measured by P-3B and a given sonde usually matched up very well. Therefore, temperature data from the two platforms were integrated together, while we further combined them with ground measurements of temperature (e.g. mobile labs) if available. The merged temperatures were grouped in bins of 100 m, and the mean value in each bin was used to make the final temperature profile.

2.3.4. Data coverage

We quantify contributions from each in-situ platform to the validation dataset using two approaches: (1) by the sum of total measurement time, and (2) by the number of cases when the platforms were collocated with IASI. Some measurements were counted more than once if they were found to be collocated with IASI in multiple windows that we tested. Figure 4 shows that the P-3B aircraft that carried the PTR-MS instrument was the largest contributor to the in-situ dataset in Colorado, because we required each IASI-in-situ collocation to have an aircraft profile from P-3B (the C-130 aircraft, on the other hand, did not perform vertical profiles at fixed locations). The Princeton mobile lab and the BAO tower were operational on most days and became the next major contributors. Although each in-situ NH_3 instrument has a different uncertainty estimate (Table 1), we applied a 35% error (i.e. typical PTR-MS uncertainty) to the entire in-situ dataset to approximate the overall instrument uncertainty. Because of potential systematic biases in the in-situ measurements, we did not use a weighted average of errors from different measurements within a given profile layer. Instrument biases were thought to be the limiting factors of the uncertainty in all the in-situ measurements of NH_3 mixing ratio, and unlike random errors, these would not be reduced through averaging.

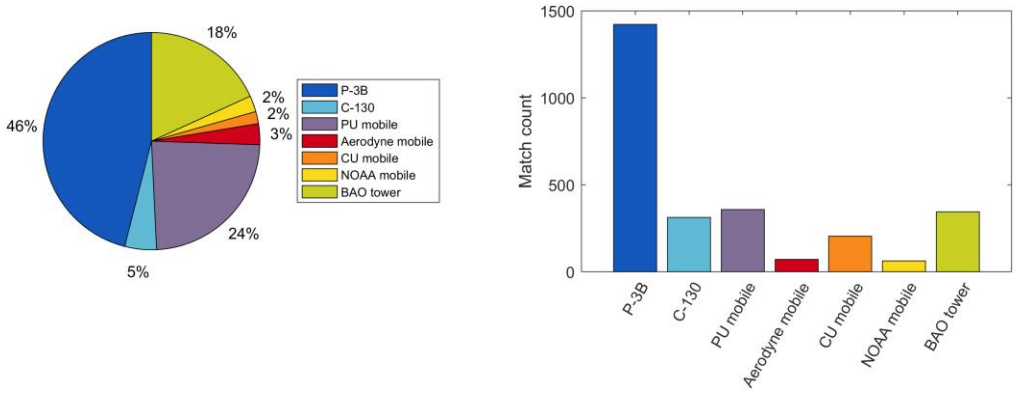

Figure 4. Data contribution from each in-situ platform in DISCOVER-AQ Colorado by (a) sum of total measurement time (1,996 hours) and (b) number of cases collocated with IASI. Statistics shown here are for all nine spatiotemporal windows tested in this study (1,426 total matches, including overlapping cases among different windows).

3. Results and Discussion

3.1. Comparison between Different In-situ Profiles

The average wind speed at 300 m measured from the BAO tower during the campaign was 3.5±2.2 m s^{-1} (median: 3.1 m s^{-1}). The mean value is equivalent to a spatial window of approximately 15 km in diameter on an hourly scale. While we recognize that wind conditions may vary slightly among different regimes, a spatial window of ±15 km around the IASI centroids and a temporal window ±60 min around the overpass times were internally consistent

with one another and can be used to account for the transport of NH_3 under typical atmospheric conditions during this period.

Within the ±15 km and ±60 min spatiotemporal window, the four different scenarios of NH_3 profiles were quantitatively evaluated and compared based on the data in Colorado, given the larger suite of measurements in this campaign. For comparison purposes, we only show the comparison between in-situ and the reanalysis IASI product, but the overall conclusions hold for the other two IASI products as well. The IASI reanalysis product versus the four in-situ profiles are plotted in Figure 5 with an orthogonal linear regression fit (lsqfitma, https://www.mbari.org/index-of-downloadable-files/) that minimizes the perpendicular distances to the fitted line from the abscissa and ordinate variables simultaneously. We did not force the intercept through zero because the IASI instrument has a detection limit (Van Damme *et al.*, 2014), and therefore a non-zero intercept is more reasonable and realistic in representing the sensitivity of IASI towards in-situ data. Profile 1 leads to the lowest column abundances among the four profiles because all the NH_3 measurements above the MLH are excluded. The column abundances increase sequentially from profile 1 to 4 as the contributions from the free troposphere increase. In theory, the MLH assumption (profile 1) would be the closest representation of vertical distributions of NH_3 in the real atmosphere based on its short lifetime, emissions at the surface, and negligible amounts measured elsewhere in the free troposphere. The correlation coefficient and slope between IASI and in-situ data in Colorado indeed show a sequential degradation from profile 1 to 4 as extra NH_3 is added into the integration. Profile 1 shows the overall best agreement between IASI and in-situ, and this is consistent with the expectation that most NH_3 is accumulated within the boundary layer. We note that profile 2, which treats all aircraft data as valid, shows a similar correlation (though with a factor of two difference in the slope). However, there are potential caveats associated with using the airborne measurements above the MLH given the sampling artifacts, which will be discussed in detail in section 3.5. All the correlations shown are tested to be statistically significant ($p<0.05$, same for all the analyses onward).

While we calculated the MLH using three different approaches, there were many cases in which only one or two of the approaches was available, especially when using smaller spatiotemporal windows. For example, only 19 of the 63 cases shown in Figure 5 had valid MLH information from all three approaches simultaneously. The means and standard deviations of MLH in these 19 cases are as follows: B200: (2.3±0.31) km; P-3B tracers: (2.8±0.36) km; sonde: (2.7±0.24) km. These variabilities can partially be attributed to the spatial and temporal separation between the instruments, thus the reason we chose to use the average of the available approaches as the representative MLH.

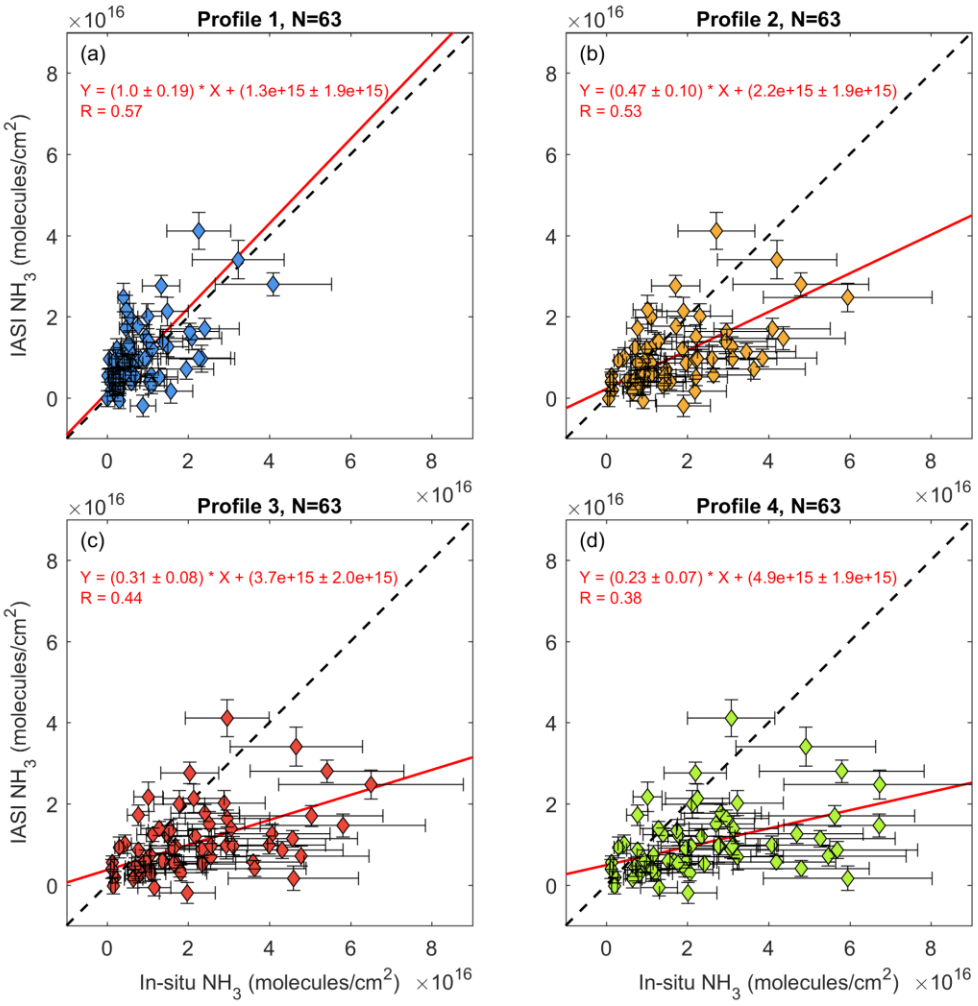

Figure 5. Reanalysis IASI product versus in-situ integrated columns from the four profiles for the ±15 km and ±60 min window in Colorado. Profile 1: integration up to MLH; Profile 2: integration up to maximum aircraft altitude; Profile 3: integration up to tropopause assuming a linearly decreasing NH_3 mixing ratio beyond aircraft altitude; Profile 4: integration up to tropopause assuming constant NH_3 beyond aircraft altitude. Error bars indicate the uncertainties of columns. Red line shows the best fit using orthogonal regression. Dashed line represents the 1:1 slope.

3.2. Comparison between Different IASI Products

The three IASI products described in section 2.1 were compared with vertically integrated in-situ columns under the MLH assumption (profile 1) within the ±15 km and ±60 min window in Colorado (Fig. 6). The near real-time product comparing with in-situ columns integrated up to the MLH and within the ±15 km and ±60 min spatiotemporal window yielded a correlation coefficient of 0.58, an intercept of $(2.1\pm1.5)\times10^{15}$ molecules cm^{-2} and a slope of 0.78±0.14. The reanalysis product showed no real changes in the correlation coefficient (0.57) and intercept ($(1.3\pm1.9)\times10^{15}$ molecules cm^{-2}), but a slope closer to unity (1.0±0.19) was observed. The in-situ derived IASI product showed a similar correlation (0.54), slope (1.1±0.22)

and intercept ($(1.7\pm2.2)\times10^{15}$ molecules cm^{-2}). All the correlations are statistically significant. The intercepts for the three products are nearly indistinguishable from zero, particularly when compared to column amounts > 10^{16} molecules cm^{-2}, suggesting that there is no significant absolute bias between the IASI and in-situ datasets.

Accurate temperature measurements are needed for NH_3 retrievals, especially in the lower layers of the atmosphere where errors in the temperature profile can affect the retrieved NH_3 columns significantly. The reanalysis product relies on gridded ECMWF meteorological data, and our results showed the robustness of this implementation, which allows for long-term consistent time series of IASI. The in-situ derived IASI product shows a slightly deviated slope from unity, but the fact that this product matched well with the reanalysis product (Fig. 6d) suggests that the retrievals are still internally coherent. The deviation may be attributed to the fact that the in-situ temperature profiles largely consisted of sonde data, and sonde measurements were not always representative of the IASI pixel in space and time. Our results are also consistent with previous findings that the historic version 2.1 near real-time product (before September 30, 2014 and the release of the IASI L2 version 6.0.5 by EUMETSAT) has a low bias against the reanalysis product due to an overestimation of the thermal contrasts between the surface and the lower tropospheric air (Van Damme *et al.*, 2017). The differences in temperature inputs are further illustrated in Figure 7, where we plot the mean temperature profile used in the retrieval of each IASI product (left panel) and an example of a single observation (right panel). The different profile shapes and thermal contrast values explain why the retrieved column abundances vary. The largest thermal contrast (TC, shown as inset) between the surface air temperature and skin temperature (i.e. soil temperature) is found in the near real-time product, confirming the reason why the retrieved columns are biased low against the other two products.

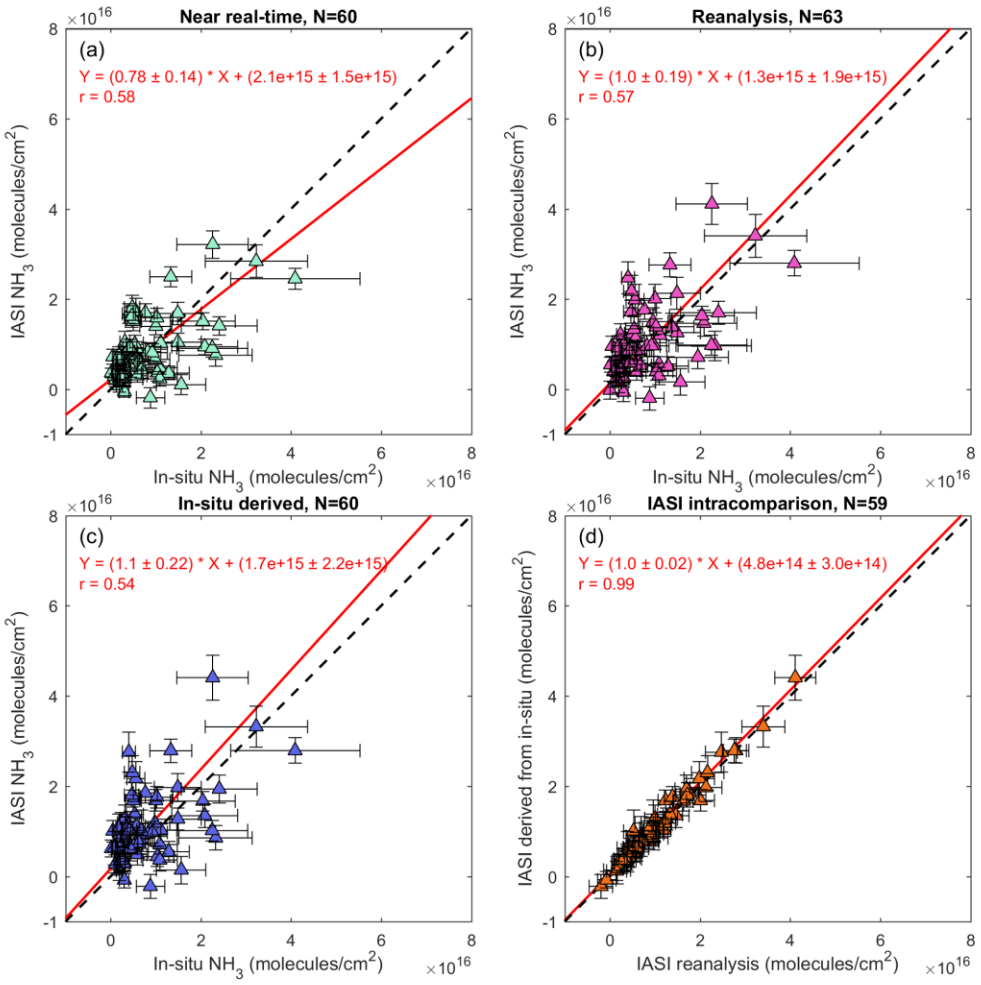

Figure 6. IASI-NH_3 products (a. near real-time, b. reanalysis, c. in-situ derived) versus the in-situ NH_3 columns in Colorado based on the ±15 km and ±60 min window and MLH assumption. The intracomparison between the reanalysis and in-situ derived IASI products is shown in (d). Red line shows the best fit using orthogonal regression. Dashed line represents the 1:1 slope.

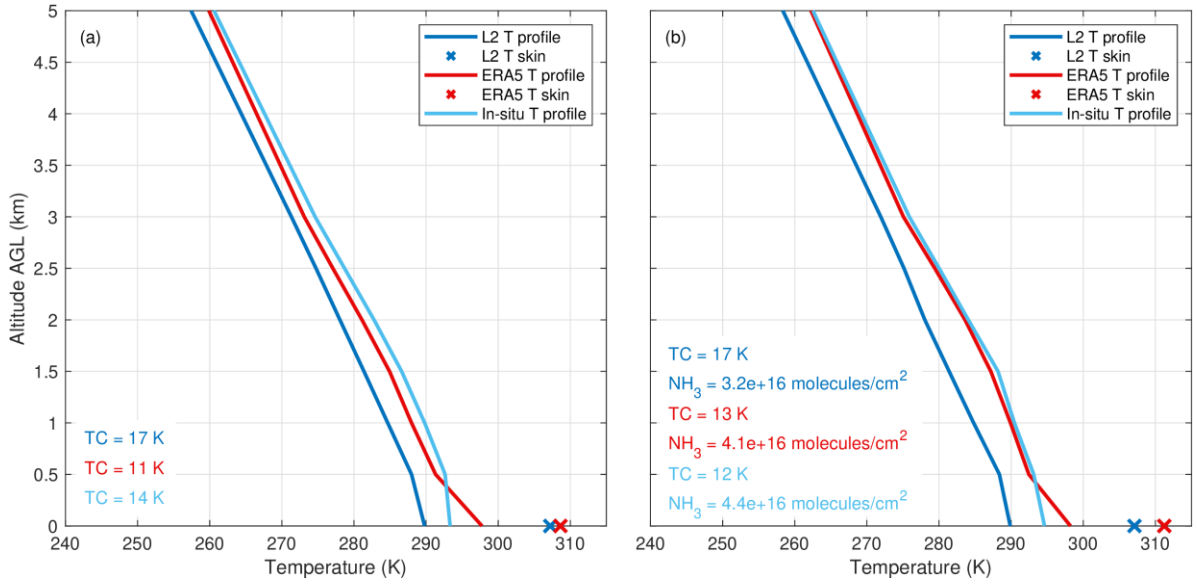

Figure 7. EUMETSAT L2 (dark blue), ERA5 (red) and in situ (light blue) temperature profiles used in the retrieval of the near real-time, reanalysis and in-situ derived IASI products. Left panel: mean temperature profile in this study; right panel: a single observation on Aug 3, 2014 from IASI MetOp-A (39.867° N, 105.205° W).

While linear regression provides a straightforward picture of how two datasets relate with each other, the fitted slopes and intercepts can be driven by outliers on either side. We additionally calculated histograms to check for potential differences that may exist between the IASI and in-situ measurements. The remainders obtained from subtracting in-situ columns from corresponding IASI columns are illustrated in Figure 8 (same scenarios as Fig. 6: IASI products versus the in-situ MLH assumption for the ±15 km and ±60 min window in Colorado). The Freedman-Diaconis rule was used to calculate the appropriate bin width and number of bins for each distribution (Freedman & Diaconis, 1981). A Gaussian function was used to fit the remainders for a smoother interpretation of distribution. The histograms show that the remainders were clustered around zero for all three products, with the near real-time product having the smallest mean. This again indicates that the IASI products do not appear to have large systematic biases. Therefore, averaging IASI observations under different scenarios (low/moderate/high NH_3) likely will yield improved detection limits as any random measurement noise becomes averaged out.

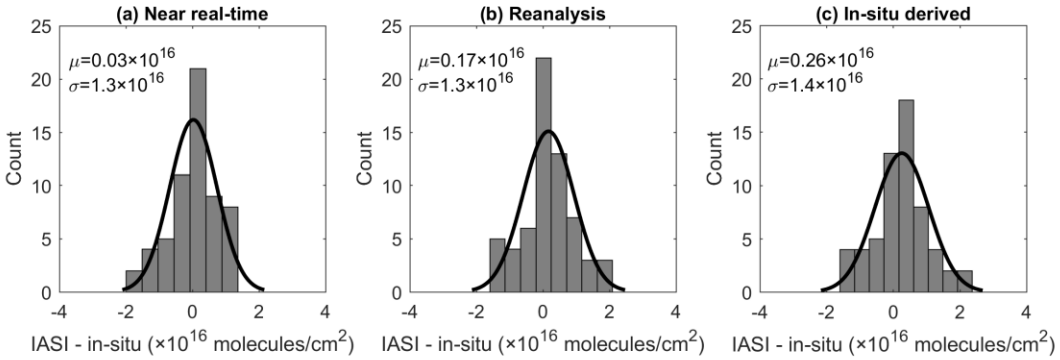

Figure 8. Histograms showing the remainders between IASI and in-situ NH_3 columns in Colorado (±15 km, ±60 min window, MLH assumption) for (a) the near real-time, (b) the reanalysis and (c) the in-situ derived products. The fitted Gaussian distribution is plotted as a black curve. μ and σ denote the mean and standard deviation of the fitted Gaussian function, respectively.

3.3. Comparison between Colorado and California

The DISCOVER-AQ California campaign was conducted over the San Joaquin Valley, the most productive agricultural region in the U.S., with Kern County and Tulare County ranking top in total value of production as of 2017 (CDFA, 2018). Previous studies have found significantly high NH_3 abundances in the San Joaquin Valley (Clarisse *et al.*, 2010; Makar *et al.*, 2009), making it a suitable area to evaluate the sensitivity of IASI towards surface NH_3. However, using the same criteria as for Colorado, only a limited number of collocated case (N=3, 9, 4 for near real-time, reanalysis and in-situ derived products) were found in California. Part of the reason was that only the MetOp-A satellite was available during that time, whereas both MetOp-A and B were operational during the Colorado campaign. The main factor, however, was that the California campaign happened during winter in a valley area, where high cloud coverage, low thermal contrast and strong but shallow temperature inversions were frequently present. These conditions pose a challenge for accurate satellite NH_3 retrievals from an infrared sounder. For demonstration purposes, a test was conducted from January 16 to February 7, 2013 to retrieve NH_3 columns for all the IASI MetOp-A pixels within the DISCOVER-AQ California domain. Using the near real-time product as an example, only 22% of pixels produced valid columns after filtering for cloud (< 25%), accounting for the availability of skin temperature and applying post-filtering, a process that was used to remove erroneous retrievals (Van Damme *et al.*, 2017). In contrast, a similar test between July 17 and August 10, 2014 over the DISCOVER-AQ Colorado domain showed that 51% of the MetOp-A and B pixels remained after the quality control process. The limited sample size makes it extremely difficult to draw any conclusions on the agreement between IASI and in-situ measurements in California. Given this, the scope of this study is limited to Colorado. Table S2 lists the orthogonal regression results between the IASI reanalysis product and the in-situ MLH assumption in California for all the spatiotemporal windows we tested. The California example highlights the fact that validation results in one area may not apply to another area, especially where the conditions are dramatically different for satellite observations. Similar to the results in Colorado, the reanalysis product in California yielded more datapoints because of the increased availability of temperature profiles.

3.4. Comparison Between Spatiotemporal Windows

As described in section 3.1, we used the ±15 km spatial window in conjunction with the ±60 min temporal window to account for the transport of NH_3 based on the typical boundary layer wind speed of 3.5±2.2 m s^{-1}. We also evaluated the sensitivity of agreement between IASI and in-situ data using other combinations of spatiotemporal windows up to a factor of three apart in space and time. Table 3 lists the orthogonal regression results between IASI and the in-situ MLH assumption under nine different spatiotemporal windows. The near real-time IASI product is shown here as an example. For statistics of the other two IASI products, we refer to Table S3 and S4. The correlations in all nine windows are tested to be statistically significant. Aside from the ±15 km and ±60 min window that has been adopted throughout the analysis, the ±15 km and ±20 min window also showed similar performance. The "within pixel" and ±20 min window even outperforms the original window in terms of slope and correlation, which is reasonable since we expect that most NH_3 emitted will not drift far from their source in such a short time frame. However, it should be noted that the ±15 km and ±60 min window has a much larger sample size than the two windows above, providing higher statistical power. From a statistical perspective, none of the remaining windows are comparable to the ones discussed in terms of overall agreement.

Table 3. *Orthogonal regression statistics between the near real-time IASI product and the in-situ MLH assumption in Colorado for all the spatiotemporal windows tested, including overlapping points*

Temporal window	20 min			60 min			180 min		
Spatial window	Within pixel	15 km	45 km	Within pixel	15 km	45 km	Within pixel	15 km	45 km
Slope	0.93 ±0.17	0.76 ±0.17	0.09 ±0.03	2.1 ±0.72	0.78 ±0.14	0.85 ±0.13	2.3 ±0.50	2.7 ±0.66	0.42 ±0.06
Intercept	8.0e14 ±2.4e15	1.2e15 ±2.7e15	7.5e15 ±6.4e14	-4.7e15 ±5.1e15	2.1e15 ±1.5e15	1.3e15 ±1.0e15	-3.9e15 ±3.2e15	-7.9e15 ±4.4e15	4.2e15 ±5.1e14
Correlation coefficient	0.84	0.68	0.22	0.50	0.58	0.38	0.64	0.41	0.38
Number of datapoints	12	22	152	25	60	244	32	81	259
IASI mean	1.1e16 ±9.7e15	1.1e16 ±9.2e15	8.4e15 ±6.9e15	9.2e15 ±7.6e15	8.8e15 ±7.1e15	7.1e15 ±6.4e15	9.4e15 ±7.8e15	9.2e15 ±8.0e15	6.7e15 ±5.8e15
In-situ mean	1.1e16 ±1.0e16	1.3e16 ±1.1e16	1.0e16 ±1.9e16	6.6e15 ±5.1e15	8.5e15 ±8.2e15	6.8e15 ±6.8e15	5.7e15 ±4.4e15	6.3e15 ±5.0e15	5.9e15 ±8.4e15
% difference	0.60	-15	-18	39	3.1	4.0	66	46	13

Note. "Within pixel" means that the in-situ measurements must be located within the actual IASI pixel (~ 12 km in diameter). Standard deviations are shown for slopes, intercepts and means. The last row shows the percent difference between the means of IASI and in-situ columns.

3.5. Ascent and Descent Aircraft Profiles

An earlier study on the validation of TES NH_3 suggested that the two airborne NH_3 sensors (PTR-MS and CRDS) in DISCOVER-AQ California exhibited hysteresis during

sampling (Sun *et al.*, 2015). In Figure 2b and c of Sun *et al.* (2015), the measured NH_3 concentrations showed long tails of decay when exiting the boundary layer into the free troposphere due to the sensors' relatively long response times. On the other hand, the sensors detected almost no NH_3 signals when descending from the free troposphere until reaching the boundary layer, likely affected by an extended portion of outgassing in clean conditions prior to the descent. The Colorado campaign only had PTR-MS onboard the P-3B aircraft, but here we also examined the differences between the ascent and descent profiles. We remind that the PTR-MS had limitations in detection limit and response time because it was not optimized for measuring NH_3 at the time of DISCOVER-AQ.

As an example of the hysteresis in sampling, we selected two pairs of locations relatively close to each other where aircraft profiling was conducted to minimize the influence of NH_3 gradients across the transect. Figure 9a shows the time series on July 23, 2014, of NH_3 for an ascent profile at NREL (Golden), a high-altitude leg near 5.5 km MSL for 22 km (2.5 min) and then a descent spiral profile near the BAO tower (near Erie). The second pair of profiles consisted of an ascent at Denver (La Casa), another high-altitude segment at 5.5 km MSL for 26 km (3 min), followed by a descent at Chatfield Park south of Denver. MLH was estimated from the P-3B aircraft temperature profiles and found to be similar between these locations (difference within 100 m). The geographical locations of the four sites are shown in Figure 9b.

Figure 9c and d show the vertical profiles of NH_3 for the near-adjacent ascent and descent pairs. For comparison, Figure 9e and f show the same pairs of profiles for C_2H_6, a petrochemical tracer with a ~ 2 month lifetime that has sources located in the same general areas as NH_3 emissions in northeast Colorado and has no sampling issues (Kille *et al.*, 2019). The dashed line marks the average boundary layer height averaged between each pair. For the first set of profiles (Fig. 9c), the descent had an average NH_3 mixing ratio of 2.2 ppbv while the ascent averaged over two times higher at 4.6 ppbv. We hypothesize these differences were mainly due to instrument sampling issues because the corresponding C_2H_6 profiles (Fig. 9e) showed no noticeable differences between the two sites, particularly the relative shapes of the profiles around the MLH. This sampling hysteresis for NH_3 is consistent with those reported by Sun *et al.* (2015). We investigated several other profiles and found similar patterns, especially when there were large enhancements of NH_3 (> 5 ppbv) near the ground, suggesting that PTR-MS was subject to artifacts because the instrument was not optimized for sampling and detecting NH_3.

For the second pair (Fig. 9d), the average NH_3 during descent again was lower than the ascent, but there was a difference in air mass between these two sites. Figure 9f shows that C_2H_6 had different boundary layer profiles in the two locations, though were indistinguishable at and above it. Nonetheless, the relative shapes of the NH_3 and C_2H_6 profiles are dramatically different, with C_2H_6 showing an abrupt and large decrease above the MLH while NH_3 shows a more gradual decrease around the MLH. The more gradual transition of NH_3 is again likely related to sampling biases, though real air mass differences certainly play some role at least in the boundary layer.

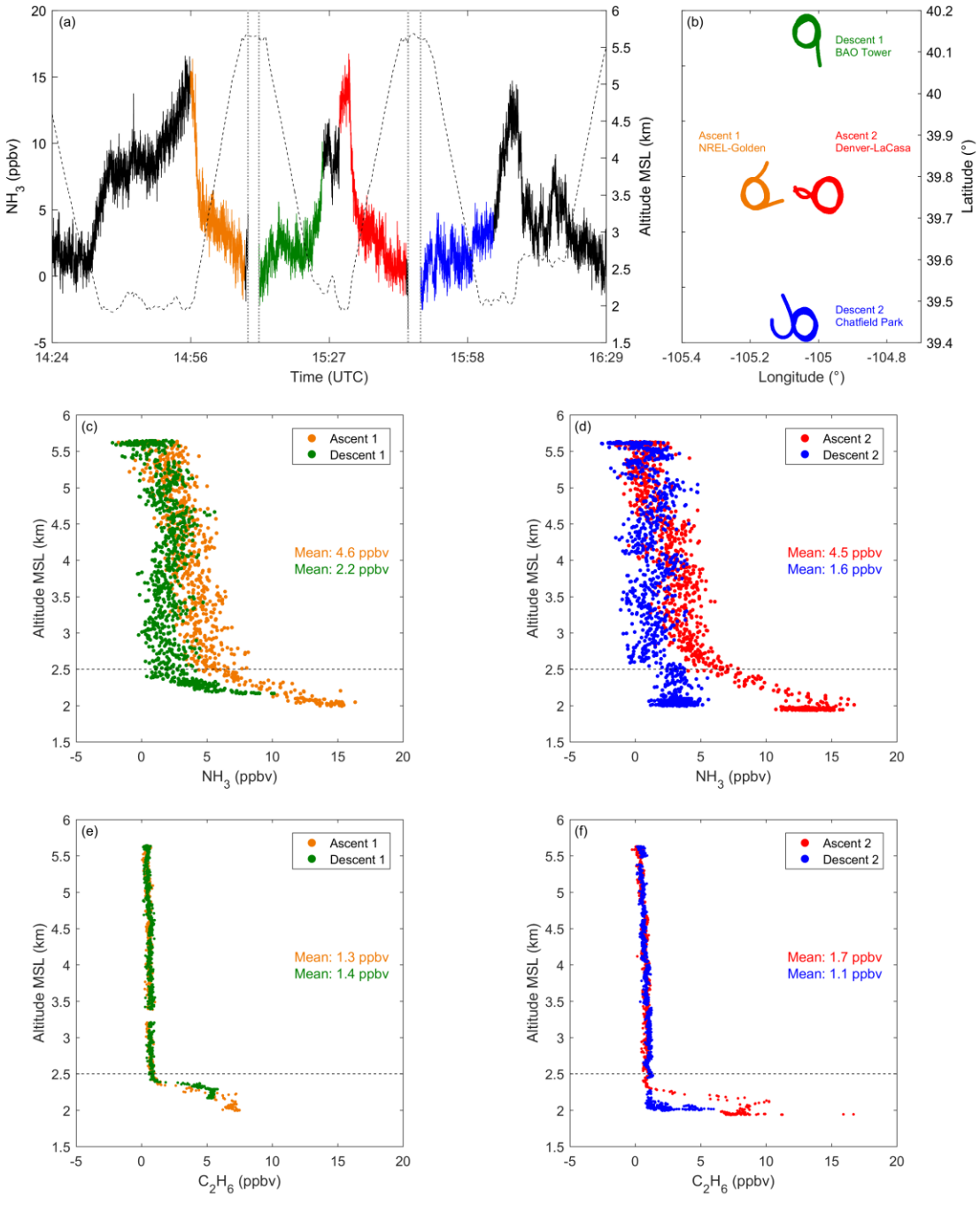

668

669 **Figure 9**. Vertical profiles of 1 Hz NH_3 and C_2H_6 measurements from the P-3B aircraft in
670 Colorado on July 23, 2014. Panel (a) shows the time series of NH_3 measured by the PTR-MS.
671 The two pairs of adjacent ascent and descent profiles selected for comparison are highlighted by
672 different colors. The thin dashed line and grey dotted vertical lines show the altitude change
673 during the flight and breaks in the time series, respectively. Panel (b) shows the geographical
674 locations where the aircraft profiles were made. Panels (c) and (d) illustrate the NH_3 profiles
675 during the ascents and descents. Dashed lines mark the MLH averaged across each ascent and

descent pair. Panels (e) and (f) are the corresponding C_2H_6 profiles measured simultaneously by a TILDAS instrument.

While we have demonstrated that IASI is comparable to in-situ-derived profiles in general, the differences between ascent and descent profiles due to sampling issues require more examination. We show in Figure 10 the comparison of the three IASI products against ascents and descents separately, and key differences are readily observed. For example, the ascent profiles yield higher columns than corresponding IASI columns, consistent with the above observations of instrument artifacts from outgassing. Likewise, descent profiles are generally lower due to surface adsorption upon rapid increases in NH_3 concentrations as one descends. As a result, the descent clusters have higher slopes than the ascent clusters. Descents tend to have much higher correlations than ascents (0.62-0.68 vs. 0.43-0.46) as well as slopes closer to unity, but their intercepts also tend to be larger. Because sampling biases occur after large concentration changes regardless of the direction (net adsorption vs. net outgassing), it is unclear which of these profiles is more representative of the actual distribution. Therefore, we have opted to aggregate all PTR-MS measurements together regardless of the flight direction. Our findings suggest that attention needs to be paid to the discrepancies between ascent and descent profiles as a metric of in-situ, instrument inlet/sampling performance. Future airborne campaigns targeting NH_3 concentrations should employ sensors with highly quantified instrument responses in-flight, during upward and downward flight profiles in the same location, and with high precision and low bias in order to obtain more accurate NH_3 vertical profiles.

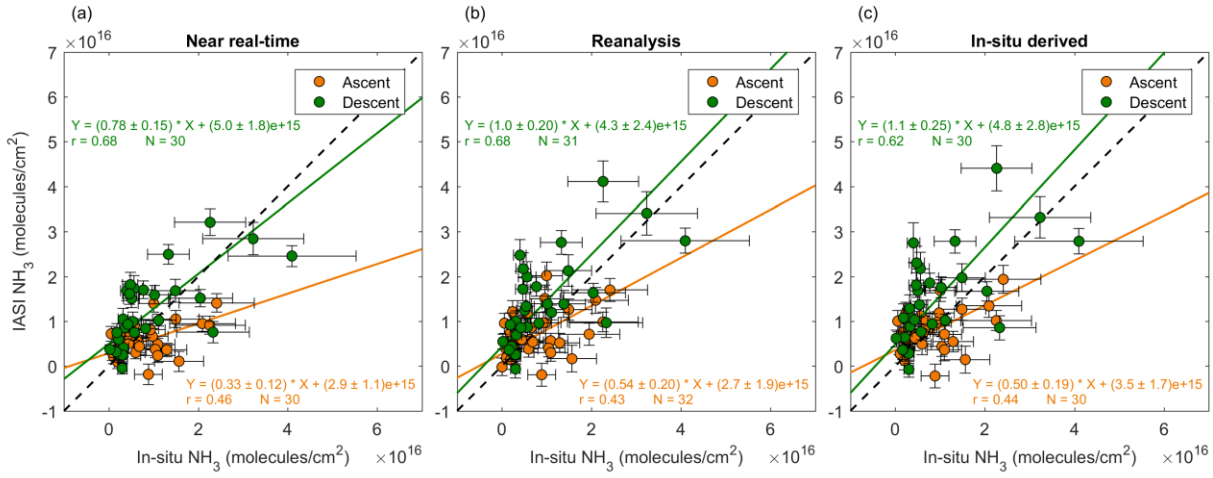

Figure 10. IASI-NH_3 products versus the in-situ NH_3 columns in Colorado (±15 km and ±60 min window and MLH assumption) with ascent (orange) and descent (green) aircraft profiles analyzed separately (same data replotted from Figure 6).

3.6. Comparison between IASI and CU SOF

Aside from in-situ NH_3 mixing ratios, ground-based mobile CU SOF measurements of NH_3 total columns were also available during the DISCOVER-AQ/FRAPPÉ Colorado campaign (Kille *et al.*, 2017). The CU SOF NH_3 columns depend only weakly on a priori parameters and have a small total uncertainty (accuracy: 4%, and not less than 0.7×10^{15} molecules cm^{-2}; Kille *et*

al., 2017, 2019). For this comparison, we removed the requirement that each collocation must have an aircraft profile and focused only on the CU SOF measurements within the ±15 km and ±60 minute window and where the CU SOF had at least partial overlap with the IASI pixel. Figure 11a shows a case study of the mobile CU SOF passing through an IASI pixel on July 28, 2014. The IASI reanalysis column and uncertainty in this case is $(9.6\pm2.2)\times10^{15}$ molecules cm^{-2}, whereas the CU SOF median and standard deviation are $(10\pm1.9)\times10^{15}$ molecules cm^{-2}, with individual values as low as $(6.0\pm0.7)\times10^{15}$ and up to $(21\pm1)\times10^{15}$ molecules cm^{-2} observed (Fig. 11b). Because the CU SOF was not fixed in space and time as it constantly moved on the road, it clearly demonstrated the high intra-pixel variability of NH_3 vertical column densities. A total of 26 cases with orthogonal regression between IASI reanalysis columns and CU SOF medians yielded a slope of unity (0.91±0.26), an intercept nearly indistinguishable from zero ($(-3.4\pm3.1)\times10^{15}$ molecules cm^{-2}), and a correlation coefficient of 0.56 (Fig. 11c). A single pixel satellite measurement inherently integrates the true NH_3 column gradients, and Kille *et al.* (2017) showed 90% variability in NH_3 column occurs on spatial scales shorter than 6 km in Northeastern Colorado. The CU SOF column data are unique, in that they integrate over boundary layer height, and do not depend on the NH_3 profile shape. The high column variability seen is consistent also with the aircraft and mobile data and highlights the intrinsic challenges of validating a short-lived primary species such as NH_3 that has strong spatial gradients, especially in hotspot regions like Northeastern Colorado. This fundamental sampling challenge of satellite validation is particularly severe, but not unique to NH_3, and has been observed for other gases (Ortega *et al.*, 2015).

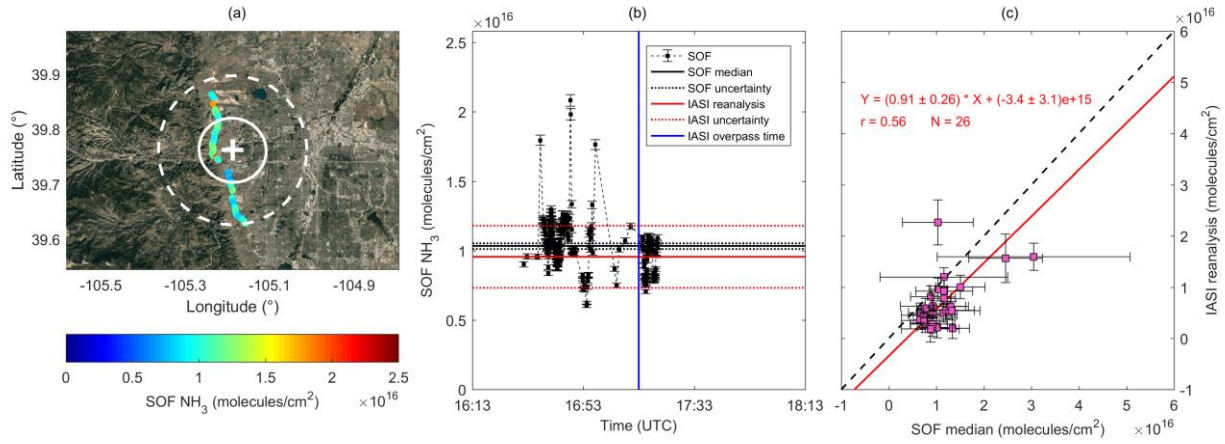

Figure 11. (a) A case study of CU SOF within the ±15 km and ±60 min window moving across the IASI pixel centroid on July 28, 2014. The route of CU SOF is colored by the measured column abundances. The center of the IASI pixel is denoted as "+". The solid ellipse marks the boundary of the IASI pixel. The dotted circle represents the ±15 km spatial window. The figure is overlaid on Google Maps. (b) Time series of CU SOF measurements in this case, with the CU SOF median and IASI reanalysis column, together with their uncertainties (see text in section 3.6), and the IASI overpass time shown. (c) CU SOF medians versus collocated IASI reanalysis columns based on the ±15 km and ±60 min window. Red line shows the best fit using orthogonal regression. Dashed line represents the 1:1 slope.

4. Implications

In the past decade, satellite NH_3 measurements have been used to study the trends and distributions of NH_3 owing to their long data record and global coverage (Dammers *et al.*, 2019; Pinder *et al.*, 2011; Van Damme *et al.*, 2018; Warner *et al.*, 2016). Although research has attempted to validate satellite NH_3 using surface concentrations and ground-based stationary FTIR measurements, the accuracy of satellite measurements on pixel scales - which are important for studying emission sources and their variabilities - has not been thoroughly validated. In this work, we compared IASI NH_3 with collocated in-situ-derived profiles and mobile SOF columns from a suite of aircraft, tower, mobile laboratory, and sonde measurements from the NASA DISCOVER-AQ and NSF FRAPPÉ field experiments. We validated version 3 of the IASI NH_3 dataset with three types of temperature profile: the near real-time product from EUMETSAT, the ERA5/ECMWF reanalysis product, and one using in-situ temperature profiles from the DISCOVER-AQ/FRAPPÉ campaign.

IASI correlates well with in-situ NH_3 integrated up to the MLH within windows of ±15 km from the IASI centroid and ±60 min of the overpass time. The choice of MLH is an important factor in this study, which determines the altitude ceiling to which in-situ data are integrated. For cases with significant NH_3 sampling biases in the free troposphere, it is recommended that the MLH information be derived from as many different approaches as possible, as some variabilities will exist among the instruments within a certain spatiotemporal window. The three IASI products show similar performances, with the reanalysis product showing the overall best agreement (slope = 1.0±0.19, intercept = $(1.3\pm1.9)\times10^{15}$ molecules cm^{-2}, r = 0.57). Because IASI has no significant biases compared to the in-situ profiles, IASI columns can be spatiotemporally averaged for improved signal to noise ratios where appropriate. The IASI retrieval depends on accurate temperature inputs, especially in the boundary layer where most NH_3 resides. The near-real time product showed a slight bias in the slope due to an overestimation of the thermal contrast relative to the reanalysis product. Our IASI results are demonstrated for summer in Colorado USA but may not be representative of other locations and times. More validations are needed, especially in cases with strong inversions and low thermal contrast such as in valleys and in winter. Large columns ($> 5\times10^{16}$ molecules cm^{-2}) could also not be validated with the current set of in situ measurements. Note that no AVK information was generated from IASI retrievals or applied to the in-situ data, and therefore this study only presents a comparison between the unconstrained IASI columns and in-situ integrated columns. A weighting function is being considered for future IASI versions that can be used to account for the variabilities of vertical sensitivity.

This study is the first validation of IASI NH_3 at the single pixel scale using vertically integrated in-situ concentrations. Nonetheless, as with TES single pixel validation results, sampling artifacts of airborne NH_3 instruments remain a significant barrier for improved validations. Not only are there fewer measurements of free tropospheric NH_3 from airborne science field campaigns compared to other in-situ trace gases, but NH_3 measurements with high accuracy and fast response are critically needed for the mapping of NH_3 vertical profiles. This is particularly important for validating in source regions where elevated concentrations in the boundary layer may influence the corresponding free tropospheric values due to sampling biases of existing instruments. Besides, vertical profiles of NH_3 in the boundary layer themselves have complex structures due to emissions, partitioning into aerosol phases, and temperature and

relative humidity changes. Until unbiased, accurate in-situ aircraft NH_3 profiles above the MLH become available, profile 1 should be used for validation as it represents a more realistic distribution of NH_3 in the troposphere. More boundary layer NH_3 profiles will improve the development of retrieval algorithms for all infrared sounders, and this can be achieved with recent advances in NH_3 measurements techniques and the increased availability of airborne research campaigns (Miller *et al.*, 2014; Pollack *et al.*, 2019).

Vertical profiles of NH_3 in the free troposphere are also a high priority, as the integrated NH_3 concentrations in the free troposphere may be comparable to the overall column abundance in low and moderate NH_3 locations. Compact spirals like those made in DISCOVER-AQ are critical for the validation of short-lived species such as NH_3 so that horizontal gradients are not manifested as vertical gradients during altitude changes. In addition, repeated upward and downward transects over the same airmass will provide a measure of confidence in any potential instrument sampling biases. While our study focuses on the measurements from IASI, these generalized conclusions hold for all infrared sounders that are sensitive to boundary layer temperature profiles and thermal contrast. Overall, more robust datasets are needed for validating satellite NH_3 measurements, particularly at the pixel scale as satellite NH_3 datasets are applied toward higher-resolution emission inventories and atmospheric composition analyses.

Acknowledgments

Xuehui Guo gratefully acknowledges the NASA Earth and Space Science Fellowship (Grant number: 80NSSC17K0377) for funding the work. We also gratefully acknowledge support for the analyses of the IASI and in-situ data products from the NASA Health and Air Quality Applied Sciences (HAQAST) team, NASA NNX16AQ90G. Mark A. Zondlo acknowledges support as a visiting scientist at ULB from the EUMETSAT Satellite Application Facility on Atmospheric Chemistry Monitoring (AC SAF). Princeton field data collection and data quality control in Colorado/California by Levi Golston and Da Pan were supported by NASA NNX14AT36G and NNX14AT32G. We acknowledge Lars Wendt, Victor Fu, Naomi Pohl, and Levi Stanton for their assistance with the Princeton field data collection in Colorado and California. Part of the research at the ULB has been supported by the IASI.Flow Prodex arrangement (ESA--BELSPO). Lieven Clarisse and Martin Van Damme are respectively a research associate and a postdoctoral researcher supported by the F.R.S.-FNRS. Cathy Clerbaux is grateful to CNES and Centre National de la Recherche Scientifique (CNRS) for financial support. IASI is a joint mission of EUMETSAT and the Centre National d'Etudes Spatiales (CNES, France). The IASI Level-1C data are distributed in near real-time by EUMETSAT through the EUMETCast distribution system. We acknowledge the AERIS data infrastructure https://www.aeris-data.fr for providing access to the IASI data as well as the NASA DISCOVER-AQ and NSF FRAPPÉ science teams, aircraft and technical crews. PTR-MS measurements during DISCOVER-AQ were supported by the Austrian Federal Ministry for Transport, Innovation and Technology (bmvit) through the Austrian Space Applications Programme (ASAP 8, #833451, #840086) of the Austrian Research Promotion Agency (FFG). Tomas Mikoviny was supported by an appointment to the NASA Postdoctoral Program at the Langley Research Center administered by Oak Ridge Associated Universities (ORAU) under contract with NASA. iMet-1 temperature soundings were provided by Anne Thompson (NASA/Goddard) and her Penn State students supported by NASA NNX10AR39G and NNX11AQ44G. UW-Madison SSEC RS92 temperature measurements were conducted by Erik

Olson. The NO_2 data on P-3B were made available by Andrew J. Weinheimer and Denise D. Montzka. The number concentrations of particles were measured by Bruce E. Anderson. The HSRL2 MLH measurements on B200 were made by Amy Jo Scarino, Chris A. Hostetler, Richard A. Ferrare and Sharon P. Burton. Rainer Volkamer acknowledges financial support for the CU SOF deployment during FRAPPÉ from the Colorado Department for Public Health and Environment (CDPHE) State of Colorado contract 14FAA64390, and US National Science Foundation (NSF) EAGER grant AGS-1452317. N.K. and Rainer Volkamer acknowledges S. Baidar, R. Sinreich, I. Ortega, P. Handley, O.W. Cooper for help during the field campaign, and J. Hannigan for access to the NCAR trailer. We also thank Cody Floerchinger and Scott C. Herndon for their contributions to the Aerodyne mobile lab measurements.

Data Availability

All the datasets used in this work are publicly available and archived at the following websites:

DISCOVER-AQ/FRAPPÉ: https://www-air.larc.nasa.gov/missions/discover-aq/discover-aq.html

IASI version 3 and 3R: https://iasi.aeris-data.fr/NH3/

References

Baidar, S., Kille, N., Ortega, I., Sinreich, R., Thomson, D., Hannigan, J., & Volkamer, R. (2016). Development of a digital mobile solar tracker. *Atmospheric Measurement Techniques*, *9*(3), 963–972. https://doi.org/10.5194/amt-9-963-2016

Bauduin, S., Clarisse, L., Clerbaux, C., Hurtmans, D., & Coheur, P. F. (2014). IASI observations of sulfur dioxide (SO2) in the boundary layer of Norilsk. *Journal of Geophysical Research: Atmospheres*, *119*(7), 4253–4263. https://doi.org/10.1002/2013JD021405

Behera, S. N., Sharma, M., Aneja, V. P., & Balasubramanian, R. (2013). Ammonia in the atmosphere: A review on emission sources, atmospheric chemistry and deposition on terrestrial bodies. *Environmental Science and Pollution Research*, *20*(11), 8092–8131. https://doi.org/10.1007/s11356-013-2051-9

Beusen, A. H. W., Bouwman, A. F., Heuberger, P. S. C., Van Drecht, G., & Van Der Hoek, K. W. (2008). Bottom-up uncertainty estimates of global ammonia emissions from global agricultural production systems. *Atmospheric Environment*, *42*(24), 6067–6077. https://doi.org/10.1016/j.atmosenv.2008.03.044

Beyersdorf, A. J., Ziemba, L. D., Chen, G., Corr, C. A., Crawford, J. H., Diskin, G. S., … Anderson, B. E. (2016). The impacts of aerosol loading, composition, and water uptake on aerosol extinction variability in the Baltimore-Washington, D.C. region. *Atmospheric Chemistry and Physics*, *16*(2), 1003–1015. https://doi.org/10.5194/acp-16-1003-2016

Bouwman, A. F., Lee, D. S., Asman, W. A. H., Dentener, F. J., Hoek, K. W. Van Der, Olivier, J. G. J., & Tg, N. (1997). A global high-resolution emission inventory for ammonia. *Global Biogeochemical Cycles*, *11*(4), 561–587.

CDFA. (2018). *California Agricultural Statistics Review 2017-2018*. Retrieved from www.cdfa.ca.gov/statistics

Clarisse, L., Clerbaux, C., Dentener, F., Hurtmans, D., & Coheur, P.-F. (2009). Global ammonia distribution derived from infrared satellite observations. *Nature Geoscience*, *2*(7), 479–483. https://doi.org/10.1038/ngeo551

Clarisse, L., Shephard, M. W., Dentener, F., Hurtmans, D., Cady-Pereira, K., Karagulian, F., … Coheur, P. F. (2010). Satellite monitoring of ammonia: A case study of the San Joaquin Valley. *Journal of Geophysical Research: Atmospheres*, *115*(13), 1–15. https://doi.org/10.1029/2009JD013291

Clerbaux, C., Boynard, A., Clarisse, L., George, M., Hadji-Lazaro, J., Herbin, H., … Coheur, P.-F. (2009). Monitoring of atmospheric composition using the thermal infrared IASI/MetOp sounder. *Atmospheric Chemistry and Physics*, *9*(16), 6041–6054. https://doi.org/10.5194/acp-9-6041-2009

Coheur, P. F., Clarisse, L., Turquety, S., Hurtmans, D., & Clerbaux, C. (2009). IASI measurements of reactive trace species in biomass burning plumes. *Atmospheric Chemistry and Physics*, *9*(15), 5655–5667. https://doi.org/10.5194/acp-9-5655-2009

Crawford, J. H., & Pickering, K. E. (2014). DISCOVER-AQ: Advancing Strategies for Air Quality Observations in the Next Decade. *Air & Waste Management Association*, 1–47. Retrieved from https://www.awma.org/content.asp?admin=Y&contentid=301

Dammers, E., McLinden, C. A., Griffin, D., Shephard, M. W., Van Der Graaf, S., Lutsch, E., … Erisman, J. W. (2019). NH3 emissions from large point sources derived from CrIS and IASI satellite observations. *Atmospheric Chemistry and Physics*, *19*(19), 12261–12293. https://doi.org/10.5194/acp-19-12261-2019

Dammers, E., Palm, M., Van Damme, M., Vigouroux, C., Smale, D., Conway, S., … Erisman, J. W. (2016). An evaluation of IASI-NH3 with ground-based Fourier transform infrared spectroscopy measurements. *Atmospheric Chemistry and Physics*, *16*, 10351–10368. https://doi.org/10.5194/acp-16-10351-2016

Dammers, E., Shephard, M. W., Palm, M., Cady-Pereira, K., Capps, S., Lutsch, E., … Willem Erisman, J. (2017). Validation of the CrIS fast physical NH3 retrieval with ground-based FTIR. *Atmospheric Measurement Techniques*, *10*(7), 2645–2667. https://doi.org/10.5194/amt-10-2645-2017

Dammers, E., Vigouroux, C., Palm, M., Mahieu, E., Warneke, T., Smale, D., … Erisman, J. W. (2015). Retrieval of ammonia from ground-based FTIR solar spectra. *Atmospheric Chemistry and Physics*, *15*(22), 12789–12803. https://doi.org/10.5194/acp-15-12789-2015

Dentener, F. J., & Crutzen, P. J. (1994). A three-dimensional model of the global ammonia cycle. *Journal of Atmospheric Chemistry*, *19*(4), 331–369. https://doi.org/10.1007/BF00694492

Eilerman, S. J., Peischl, J., Neuman, J. A., Ryerson, T. B., Aikin, K. C., Holloway, M. W., … Herndon, S. (2016). Characterization of Ammonia, Methane, and Nitrous Oxide Emissions from Concentrated Animal Feeding Operations in Northeastern Colorado. *Environmental Science and Technology*, *50*(20), 10885–10893. https://doi.org/10.1021/acs.est.6b02851

Ellis, R. A., Murphy, J. G., Pattey, E., Van Haarlem, R., O'Brien, J. M., & Herndon, S. C. (2010). Characterizing a Quantum Cascade Tunable Infrared Laser Differential Absorption Spectrometer (QC-TILDAS) for measurements of atmospheric ammonia. *Atmospheric Measurement Techniques*, *3*(2), 397–406. https://doi.org/10.5194/amt-3-397-2010

Erisman, J. W., Sutton, M. A., Galloway, J., Klimont, Z., & Winiwarter, W. (2008). How a century of ammonia synthesis changed the world. *Nature Geoscience*, *1*(10), 636–639. https://doi.org/10.1038/ngeo325

Fehsenfeld, F. C., Huey, L. G., Leibrock, E., Dissly, R., Williams, E., Ryerson, T. B., … Hartsell, B. (2002). Results from an informal intercomparison of ammonia measurement techniques. *Journal of Geophysical Research: Atmospheres*, *107*(24), 1–15. https://doi.org/10.1029/2001JD001327

Flocke, F., Pfister, G., Crawford, J. H., Pickering, K. E., Pierce, G., Bon, D., & Reddy, P. (2020). Air Quality in the Northern Colorado Front Range Metro Area: The Front Range Air Pollution and Photochemistry Éxperiment (FRAPPÉ). *Journal of Geophysical Research: Atmospheres*, *125*(2), e2019JD031197. https://doi.org/https://doi.org/10.1029/2019JD031197

Follette-Cook, M. B., Pickering, K. E., Crawford, J. H., Duncan, B. N., Loughner, C. P., Diskin, G. S., … Weinheimer, A. J. (2015). Spatial and temporal variability of trace gas columns derived from WRF/Chem regional model output: Planning for geostationary observations of atmospheric composition. *Atmospheric Environment*, *118*, 28–44. https://doi.org/10.1016/j.atmosenv.2015.07.024

Fortems-Cheiney, A., Dufour, G., Hamaoui-Laguel, L., Foret, G., Siour, G., Van Damme, M., … Beekmann, M. (2016). Unaccounted variability in NH3 agricultural sources detected by IASI contributing to European spring haze episode. *Geophysical Research Letters*, *43*(10), 5475–5482. https://doi.org/10.1002/2016GL069361

Franco, B., Clarisse, L., Stavrakou, T., Müller, J. F., Van Damme, M., Whitburn, S., … Coheur, P. F. (2018). A General Framework for Global Retrievals of Trace Gases From IASI: Application to Methanol, Formic Acid, and PAN. *Journal of Geophysical Research: Atmospheres*, *123*(24), 13,963-13,984. https://doi.org/10.1029/2018JD029633

Freedman, D., & Diaconis, P. (1981). On the histogram as a density estimator:L2 theory. *Zeitschrift Für Wahrscheinlichkeitstheorie Und Verwandte Gebiete*, *57*(4), 453–476. https://doi.org/10.1007/BF01025868

Galloway, J. N., Dentener, F. J., Capone, D. G., Boyer, E. W., Howarth, R. W., Seitzinger, S. P., … Vöosmarty, C. J. (2004). Nitrogen Cycles: Past, Present, and Future. *Biogeochemistry*, *70*(2), 153–226. https://doi.org/10.1007/s10533-004-0370-0

Golston, L. M., Pan, D., Sun, K., Tao, L., Zondlo, M. A., Eilerman, S. J., … Floerchinger, C. (2020). Variability of Ammonia and Methane Emissions from Animal Feeding Operations in Northeastern Colorado. *Environmental Science and Technology*, *54*(18), 11015–11024. https://doi.org/10.1021/acs.est.0c00301

Herndon, S. C., Jayne, J. T., Zahniser, M. S., Worsnop, D. R., Knighton, B., Alwine, E., … Kolb, C. E. (2005). Characterization of urban pollutant emission fluxes and ambient concentration distributions using a mobile laboratory with rapid response instrumentation. *Faraday Discussions*, *130*(0), 327–339. https://doi.org/10.1039/B500411J

Hoell, J. M., Harward, C. N., & Williams, B. S. (1980). Remote infrared heterodyne radiometer measurements of atmospheric ammonia profiles. *Geophysical Research Letters*, *7*(5), 313–316.

Höpfner, M., Ungermann, J., Borrmann, S., Wagner, R., Spang, R., Riese, M., … Wohltmann, I. (2019). Ammonium nitrate particles formed in upper troposphere from ground ammonia sources during Asian monsoons. *Nature Geoscience*, *12*(8), 608–612. https://doi.org/10.1038/s41561-019-0385-8

Höpfner, M., Volkamer, R., Grabowski, U., Grutter, M., Orphal, J., Stiller, G., … Wetzel, G. (2016). First detection of ammonia (NH3) in the Asian summer monsoon upper troposphere. *Atmospheric Chemistry and Physics*, *16*(22), 14357–14369. https://doi.org/10.5194/acp-16-14357-2016

IPCC. (2013). *Climate change 2013: The physical science basis, Intergovernmental Panel on Climate Change (Ch. 8, p. 682)*. Cambridge, United Kingdom and New York, NY, USA: Cambridge University Press.

Kille, N., Baidar, S., Handley, P., Ortega, I., Sinreich, R., Cooper, O. R., … Volkamer, R. (2017). The CU mobile Solar Occultation Flux instrument: Structure functions and emission rates of NH3, NO2 and C2H6. *Atmospheric Measurement Techniques*, *10*(1), 373–392. https://doi.org/10.5194/amt-10-373-2017

Kille, N., Chiu, R., Frey, M., Hase, F., Sha, M. K., Blumenstock, T., … Volkamer, R. (2019). Separation of Methane Emissions From Agricultural and Natural Gas Sources in the Colorado Front Range. *Geophysical Research Letters*, *46*(7), 3990–3998. https://doi.org/10.1029/2019GL082132

Lamarque, J. F., Kyle, P. P., Meinshausen, M., Riahi, K., Smith, S. J., van Vuuren, D. P., … Vitt, F. (2011). Global and regional evolution of short-lived radiatively-active gases and aerosols in the Representative Concentration Pathways. *Climatic Change*, *109*(1), 191–212. https://doi.org/10.1007/s10584-011-0155-0

Li, Y., Schichtel, B. A., Walker, J. T., Schwede, D. B., Chen, X., Lehmann, C. M. B., … Collett, J. L. (2016). Increasing importance of deposition of reduced nitrogen in the United States. *Proceedings of the National Academy of Sciences of the United States of America*, *113*(21), 5874–5879. https://doi.org/10.1073/pnas.1525736113

Makar, P. A., Moran, M. D., Zheng, Q., Cousineau, S., Sassi, M., Duhamel, A., … Bouchet, V. S. (2009). Modelling the impacts of ammonia emissions reductions on North American air quality. *Atmospheric Chemistry and Physics*, *9*(18), 7183–7212. https://doi.org/10.5194/acp-9-7183-2009

Mensink, C., & Deutsch, F. (2008). On the role of ammonia in the formation of PM2.5. *NATO Science for Peace and Security Series C: Environmental Security*, 548–556. https://doi.org/10.1007/978-1-4020-8453-9_60

Miller, D. J., Sun, K., Tao, L., Khan, M. a., & Zondlo, M. a. (2014). Open-path, quantum cascade-laser-based sensor for high-resolution atmospheric ammonia measurements. *Atmospheric Measurement Techniques*, *7*(1), 81–93. https://doi.org/10.5194/amt-7-81-2014

Miller, D. J., Sun, K., Tao, L., Pan, D., Zondlo, M. A., Nowak, J. B., … Scarino, A. J. (2015). Ammonia and methane dairy emission plumes in the San Joaquin Valley of California from individual feedlot to regional scales. *Journal of Geophysical Research: Atmospheres*, *120*(18), 9718–9738. https://doi.org/https://doi.org/10.1002/2015JD023241

Mizak, C. A., Campbell, S. W., Luther, M. E., Carnahan, R. P., Murphy, R. J., & Poor, N. D.

(2005). Below-cloud ammonia scavenging in convective thunderstorms at a coastal research site in Tampa, FL, USA. *Atmospheric Environment*, *39*(9), 1575–1584. https://doi.org/10.1016/j.atmosenv.2004.10.008

Müller, M., Mikoviny, T., Feil, S., Haidacher, S., Hanel, G., Hartungen, E., … Wisthaler, A. (2014). A compact PTR-ToF-MS instrument for airborne measurements of volatile organic compounds at high spatiotemporal resolution. *Atmospheric Measurement Techniques*, *7*(11), 3763–3772. https://doi.org/10.5194/amt-7-3763-2014

National Atmospheric Deposition Program. (2019). Ammonia Monitoring Network (AMoN). Retrieved from http://nadp.slh.wisc.edu/AMoN/

Nemitz, E., Milford, C., & Sutton, M. A. (2001). A two-layer canopy compensation point model for describing bi-directional biosphere-atmosphere exchange of ammonia. *Quarterly Journal of the Royal Meteorological Society*, *127*, 815–833.

Nowak, J. B., Neuman, J. A., Bahreini, R., Brock, C. A., Middlebrook, A. M., Wollny, A. G., … Fehsenfeld, F. C. (2010). Airborne observations of ammonia and ammonium nitrate formation over Houston, Texas. *Journal of Geophysical Research: Atmospheres*, *115*(22), 1–12. https://doi.org/10.1029/2010JD014195

Ortega, I., Koenig, T., Sinreich, R., Thomson, D., & Volkamer, R. (2015). The CU 2-D-MAX-DOAS instrument – Part 1: Retrieval of 3-D distributions of NO2 and azimuth-dependent OVOC ratios. *Atmospheric Measurement Techniques*, *8*(6), 2371–2395. https://doi.org/10.5194/amt-8-2371-2015

Ostro, B., Hu, J., Goldberg, D., Reynolds, P., Hertz, A., Bernstein, L., & Kleeman, M. J. (2015). Associations of mortality with long-term exposures to fine and ultrafine particles, species and sources: results from the california teachers study cohort. *Environmental Health Perspectives*, *123*(6), 549–556. https://doi.org/10.1289/ehp.1408565

Paulot, F., Jacob, D. J., Pinder, R. W., Bash, J. O., Travis, K., & Henze, D. K. (2014). Ammonia emissions in the United States, european union, and China derived by high-resolution inversion of ammonium wet deposition data: Interpretation with a new agricultural emissions inventory (MASAGE_NH3). *Journal of Geophysical Research: Atmospheres*, *119*(7), 4343–4364. https://doi.org/10.1002/2013JD021130

Pinder, R. W., Walker, J. T., Bash, J. O., Cady-Pereira, K. E., Henze, D. K., Luo, M., … Shephard, M. W. (2011). Quantifying spatial and seasonal variability in atmospheric ammonia with in situ and space-based observations. *Geophysical Research Letters*, *38*(4), 1–5. https://doi.org/10.1029/2010GL046146

Pollack, I. B., Lindaas, J., Robert Roscioli, J., Agnese, M., Permar, W., Hu, L., & Fischer, E. V. (2019). Evaluation of ambient ammonia measurements from a research aircraft using a closed-path QC-TILDAS operated with active continuous passivation. *Atmospheric Measurement Techniques*, *12*(7), 3717–3742. https://doi.org/10.5194/amt-12-3717-2019

Rasmussen, C. (2018). Farewell to a Pioneering Pollution Sensor. Retrieved June 3, 2020, from NASA Jet Propulsion Laboratory website: https://www.jpl.nasa.gov/news/news.php?feature=7061

Scarino, A. J., Obland, M. D., Fast, J. D., Burton, S. P., Ferrare, R. A., Hostetler, C. A., … Harper, D. B. (2014). Comparison of mixed layer heights from airborne high spectral

resolution lidar, ground-based measurements, and the WRF-Chem model during CalNex and CARES. *Atmospheric Chemistry and Physics*, *14*(11), 5547–5560. https://doi.org/10.5194/acp-14-5547-2014

Schiferl, L. D., Heald, C. L., Damme, M. Van, Clarisse, L., Clerbaux, C., Coheur, P. F., … Eilerman, S. J. (2016). Interannual variability of ammonia concentrations over the United States: Sources and implications. *Atmospheric Chemistry and Physics*, *16*(18), 12305–12328. https://doi.org/10.5194/acp-16-12305-2016

Seinfeld, J. H., & Pandis, S. N. (2016). *Atmospheric Chemistry and Physics: From Air Pollution to Climate Change, 3rd Edition*. Hoboken, NJ: John Wiley & Sons.

Shephard, M. W., & Cady-Pereira, K. E. (2015). Cross-track Infrared Sounder (CrIS) satellite observations of tropospheric ammonia. *Atmospheric Measurement Techniques*, *8*(3), 1323–1336. https://doi.org/10.5194/amt-8-1323-2015

Shephard, M. W., Cady-Pereira, K. E., Luo, M., Henze, D. K., Pinder, R. W., Walker, J. T., … Clarisse, L. (2011). TES ammonia retrieval strategy and global observations of the spatial and seasonal variability of ammonia. *Atmospheric Chemistry and Physics*, *11*(20), 10743–10763. https://doi.org/10.5194/acp-11-10743-2011

Someya, Y., Imasu, R., Shiomi, K., & Saitoh, N. (2020). Atmospheric ammonia retrieval from the TANSO-FTS/GOSAT thermal infrared sounder. *Atmospheric Measurement Techniques*, *13*(1), 309–321. https://doi.org/10.5194/amt-13-309-2020

Sun, K., Cady-Pereira, K., Miller, D. J., Tao, L., Zondlo, M. A., Nowak, J. B., … Hostetler, C. A. (2015). Validation of TES ammonia observations at the single pixel scale in the San Joaquin Valley during DISCOVER-AQ. *Journal of Geophysical Research: Atmospheres*, *120*(10), 5140–5154. https://doi.org/10.1002/2014JD022846

Sun, K., Tao, L., Miller, D. J., Pan, D., Golston, L. M., Zondlo, M. A., … Zhu, T. (2017). Vehicle Emissions as an Important Urban Ammonia Source in the United States and China. *Environmental Science and Technology*, *51*(4), 2472–2481. https://doi.org/10.1021/acs.est.6b02805

Tao, L., Sun, K., Miller, D. J., Pan, D., Golston, L. M., & Zondlo, M. a. (2015). Low-power, open-path mobile sensing platform for high-resolution measurements of greenhouse gases and air pollutants. *Applied Physics B*, 153–164. https://doi.org/10.1007/s00340-015-6069-1

Tevlin, A. G., Li, Y., Collett, J. L., McDuffie, E. E., Fischer, E. V., & Murphy, J. G. (2017). Tall Tower Vertical Profiles and Diurnal Trends of Ammonia in the Colorado Front Range. *Journal of Geophysical Research: Atmospheres*, *122*(22), 12,468-12,487. https://doi.org/10.1002/2017JD026534

Van Damme, M., Clarisse, L., Dammers, E., Liu, X., Nowak, J. B., Clerbaux, C., … Coheur, P. F. (2015). Towards validation of ammonia (NH3) measurements from the IASI satellite. *Atmospheric Measurement Techniques*, *8*(3), 1575–1591. https://doi.org/10.5194/amt-8-1575-2015

Van Damme, M., Clarisse, L., Heald, C. L., Hurtmans, D., Ngadi, Y., Clerbaux, C., … Coheur, P. F. (2014). Global distributions, time series and error characterization of atmospheric ammonia (NH3) from IASI satellite observations. *Atmospheric Chemistry and Physics*, *14*(6), 2905–2922. https://doi.org/10.5194/acp-14-2905-2014

Van Damme, M., Clarisse, L., Whitburn, S., Hadji-Lazaro, J., Hurtmans, D., Clerbaux, C., & Coheur, P. F. (2018). Industrial and agricultural ammonia point sources exposed. *Nature*, *564*(7734), 99–103. https://doi.org/10.1038/s41586-018-0747-1

Van Damme, M., Erisman, J. W., Clarisse, L., Dammers, E., Whitburn, S., Clerbaux, C., … Coheur, P.-F. (2015). Worldwide spatiotemporal atmospheric ammonia (NH3) columns variability revealed by satellite. *Geophysical Research Letters*, *42*(20), 8660–8668. https://doi.org/10.1002/2015GL065496

Van Damme, M., Whitburn, S., Clarisse, L., Clerbaux, C., Hurtmans, D., & Coheur, P. F. (2017). Version 2 of the IASI NH3 neural network retrieval algorithm: Near-real-time and reanalysed datasets. *Atmospheric Measurement Techniques*, *10*(12), 4905–4914. https://doi.org/10.5194/amt-10-4905-2017

Volkamer, R., Baidar, S., & Thomas, D. (2019). *Patent No. 10379194*. United States.

Von Bobrutzki, K., Braban, C. F., Famulari, D., Jones, S. K., Blackall, T., Smith, T. E. L., … Nemitz, E. (2010). Field inter-comparison of eleven atmospheric ammonia measurement techniques. *Atmospheric Measurement Techniques*, *3*(1), 91–112. https://doi.org/10.5194/amt-3-91-2010

Wang, J. L., Zhang, Y. H., Shao, M., & Liu, X. L. (2006). The quantitative relationship between visibility and mass concentration of PM2.5 in Beijing. *WIT Transactions on Ecology and the Environment*, *86*, 595–610. https://doi.org/10.2495/AIR06059

Warner, J. X., Dickerson, R. R., Wei, Z., Strow, L. L., Wang, Y., & Liang, Q. (2017). Increased atmospheric ammonia over the world's major agricultural areas detected from space. *Geophysical Research Letters*, *44*(6), 2875–2884. https://doi.org/10.1002/2016GL072305

Warner, J. X., Wei, Z., Larrabee Strow, L., Dickerson, R. R., & Nowak, J. B. (2016). The global tropospheric ammonia distribution as seen in the 13-year AIRS measurement record. *Atmospheric Chemistry and Physics*, *16*(8), 5467–5479. https://doi.org/10.5194/acp-16-5467-2016

Weinheimer, A. J., Walega, J. G., Ridley, B. A., Gary, B. L., Blake, D. R., Blake, N. J., … Collins, J. E. (1994). Meridional distributions of NOx, NOy, and other species in the lower stratosphere and upper troposphere during AASE II. *Geophysical Research Letters*, *21*(23), 2583–2586. https://doi.org/10.1029/94GL01897

Whitburn, S., Van Damme, M., Clarisse, L., Bauduin, S., Heald, C. L., Hadji-Lazaro, J., … Coheur, P.-F. (2016). A flexible and robust neural network IASI-NH3 retrieval algorithm. *Journal of Geophysical Research: Atmospheres*, *121*(11), 6581–6599. https://doi.org/10.1002/2016JD024828

Xu, W., Luo, X. S., Pan, Y. P., Zhang, L., Tang, A. H., Shen, J. L., … Liu, X. J. (2015). Quantifying atmospheric nitrogen deposition through a nationwide monitoring network across China. *Atmospheric Chemistry and Physics*, *15*(21), 12345–12360. https://doi.org/10.5194/acp-15-12345-2015

Yacovitch, T. I., Herndon, S. C., Roscioli, J. R., Floerchinger, C., McGovern, R. M., Agnese, M., … Kolb, C. E. (2014). Demonstration of an ethane spectrometer for methane source identification. *Environmental Science and Technology*, *48*(14), 8028–8034. https://doi.org/10.1021/es501475q

1116 Zhang, L., Chen, Y., Zhao, Y., Henze, D. K., Zhu, L., Song, Y., … Huang, B. (2018).
1117 Agricultural ammonia emissions in China: Reconciling bottom-up and top-down estimates.
1118 *Atmospheric Chemistry and Physics, 18*(1), 339–355. https://doi.org/10.5194/acp-18-339-
1119 2018

1120 Zhu, L., Henze, D. K., Cady-Pereira, K. E., Shephard, M. W., Luo, M., Pinder, R. W., … Jeong,
1121 G. R. (2013). Constraining U.S. ammonia emissions using TES remote sensing observations
1122 and the GEOS-Chem adjoint model. *Journal of Geophysical Research: Atmospheres*,
1123 *118*(8), 3355–3368. https://doi.org/10.1002/jgrd.50166

1124 Ziereis, H., & Arnold, F. (1986). Gaseous ammonia and ammonium ions in the free troposphere.
1125 *Nature*, *321*(6069), 503–505. https://doi.org/10.1038/321503a0

1126

Figure 1.

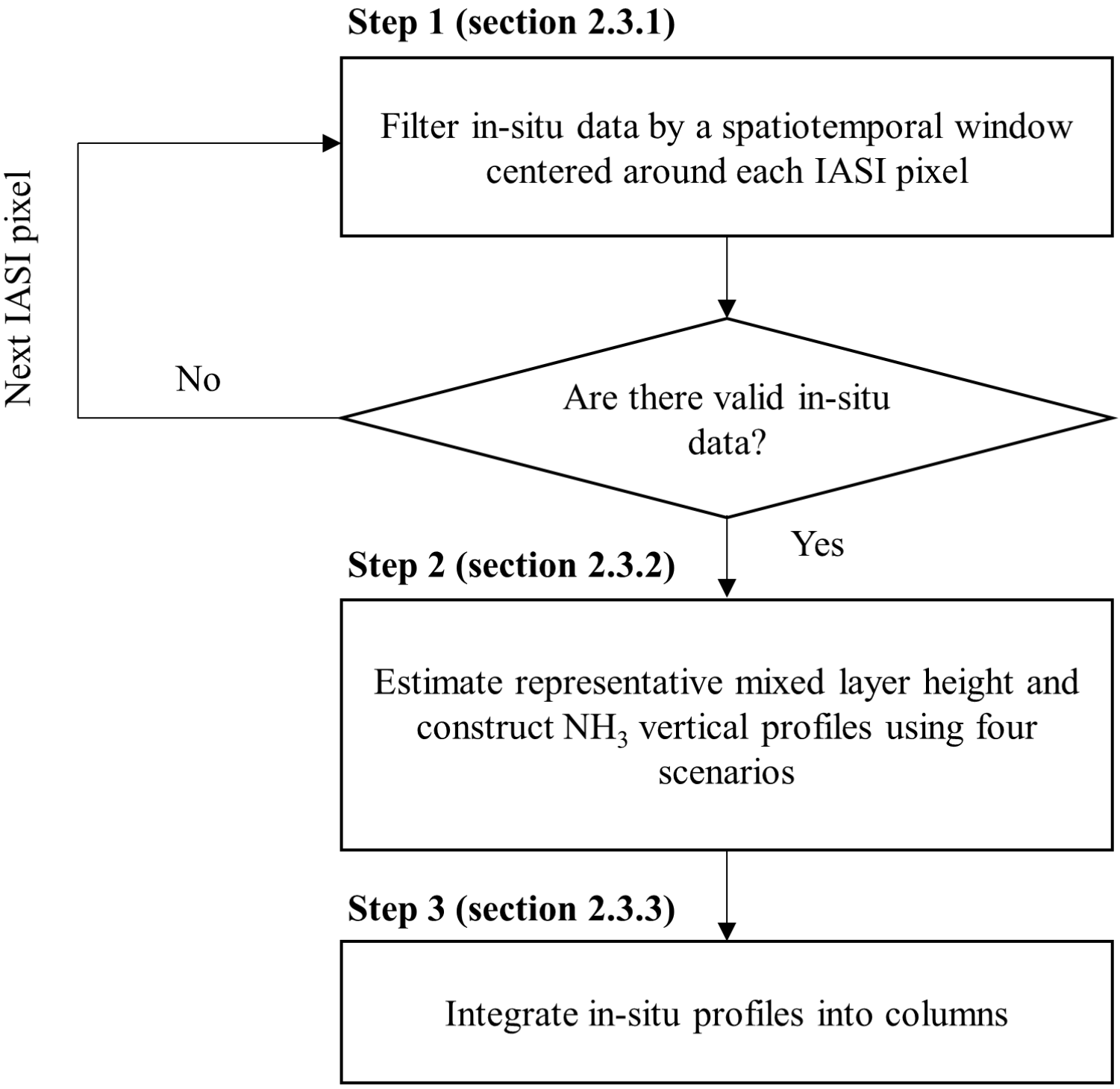
Step 1 (section 2.3.1)
Filter in-situ data by a spatiotemporal window centered around each IASI pixel
Are there valid in-situ data?
No
Next IASI pixel
Yes
Step 2 (section 2.3.2)
Estimate representative mixed layer height and construct NH_3 vertical profiles using four scenarios
Step 3 (section 2.3.3)
Integrate in-situ profiles into columns

Figure 2.

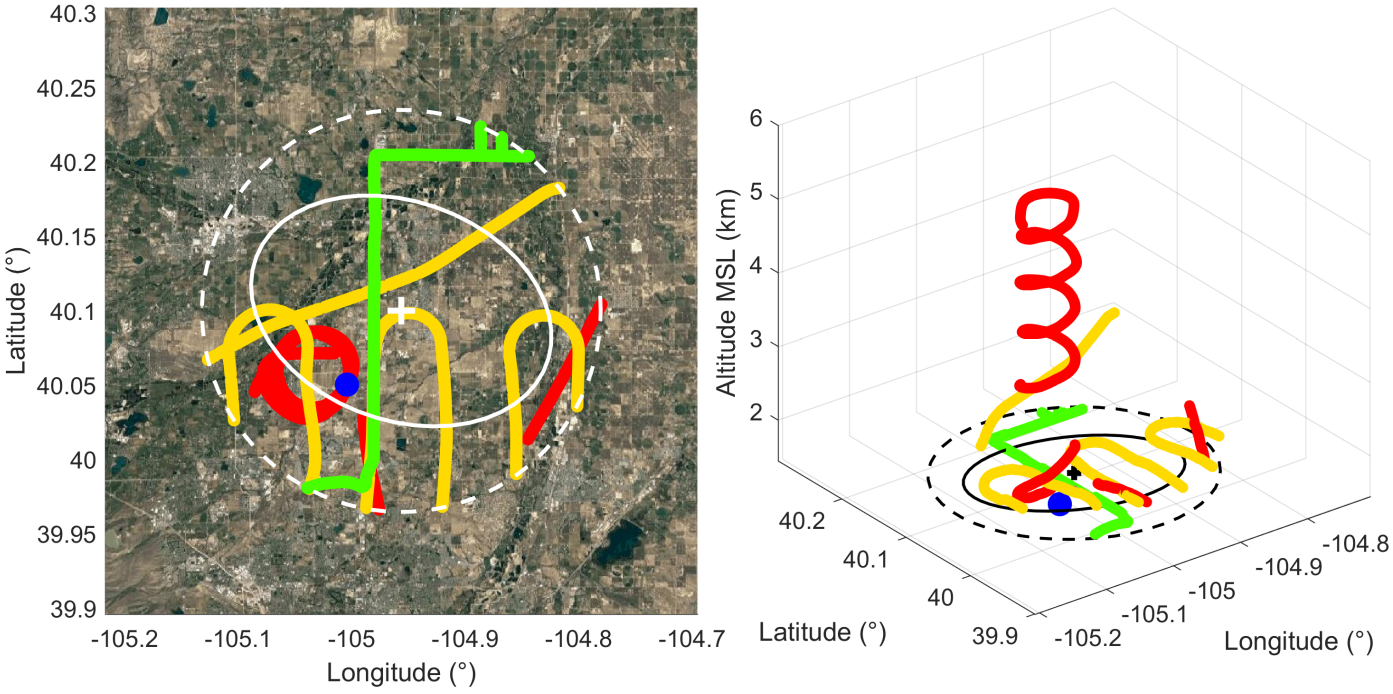
40.3
40.25
40.2
40.15
40.1
40.05
40
39.95
39.9
Latitude (°)
-105.2
-105.1
-105
-104.9
-104.8
-104.7
Longitude (°)
6
5
4
3
2
Altitude MSL (km)
40.2
40.1
40
39.9
Latitude (°)
-104.8
-104.9
-105
-105.1
-105.2
Longitude (°)

Figure 3.

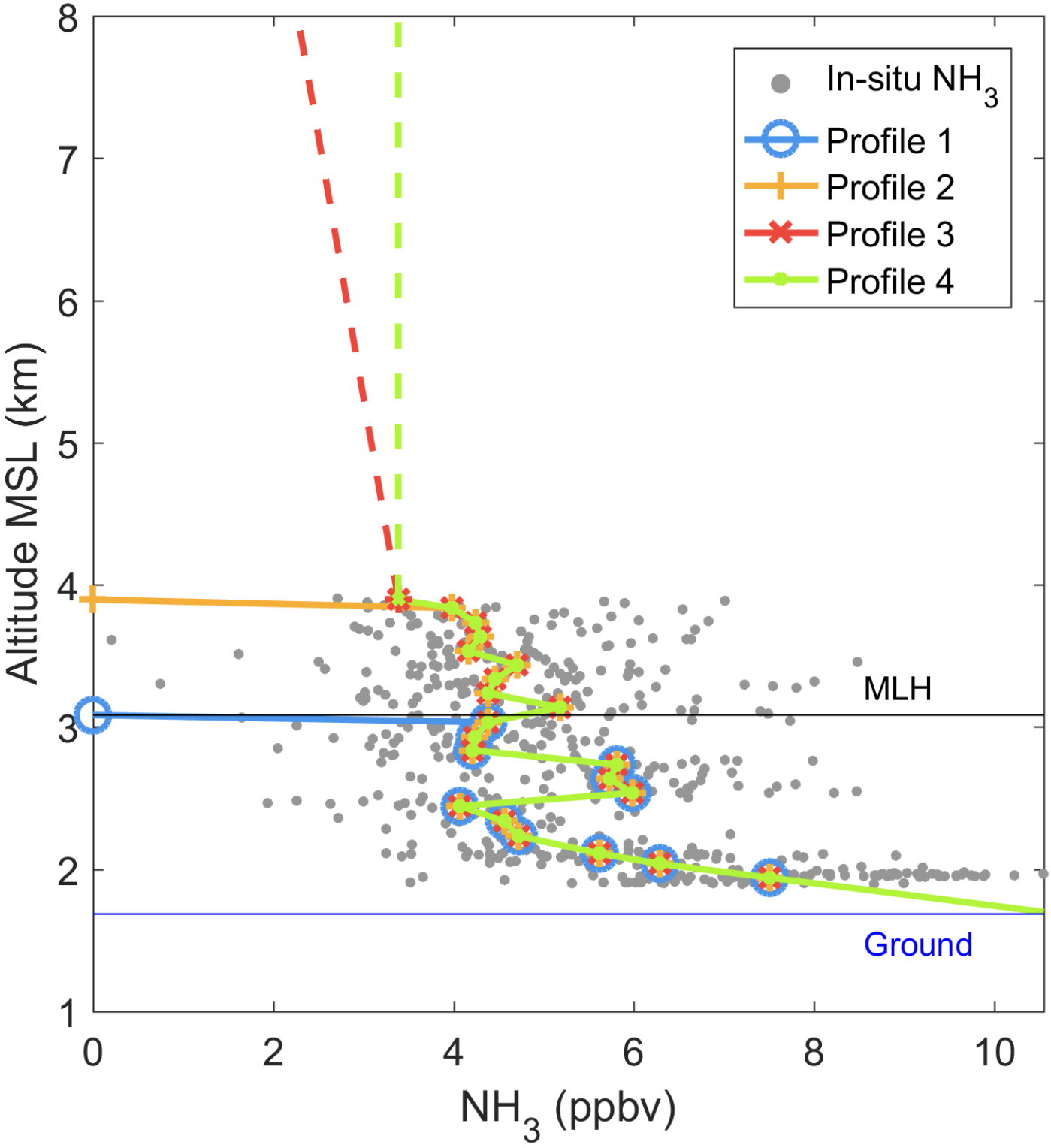
In-situ NH3
Profile 1
Profile 2
Profile 3
Profile 4
MLH
Ground
Altitude MSL (km)
NH3 (ppbv)
8
7
6
5
4
3
2
1
0
2
4
6
8
10

Figure 4.

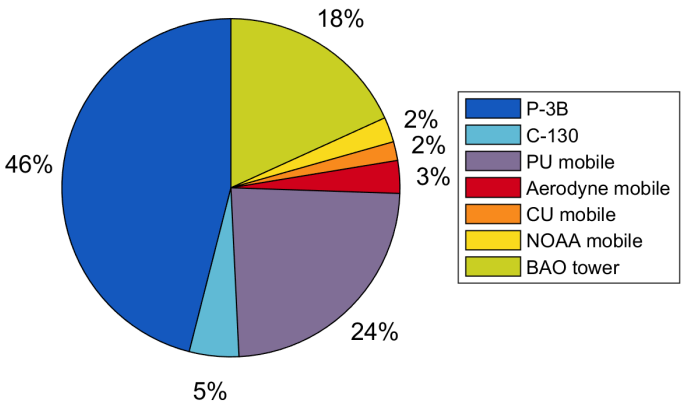
18%
2%
2%
3%
46%
24%
5%
P-3B
C-130
PU mobile
Aerodyne mobile
CU mobile
NOAA mobile
BAO tower

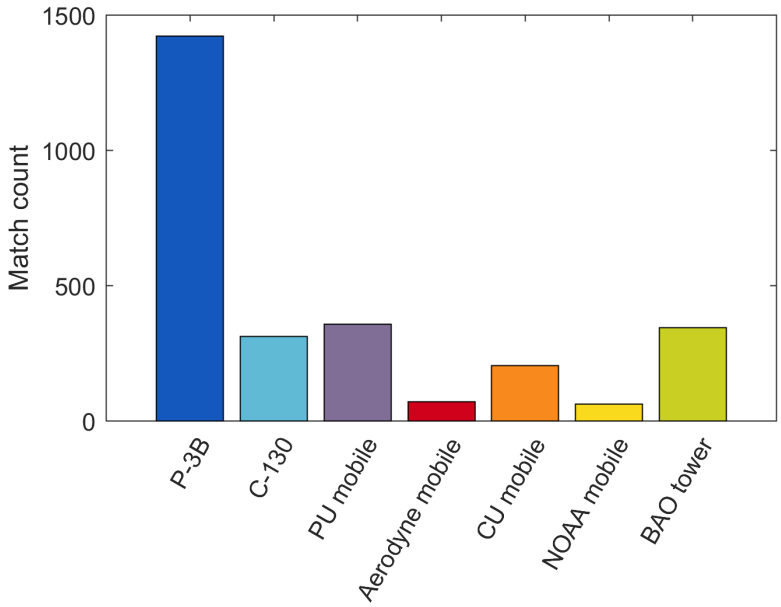
1500
1000
500
0
Match count
P-3B
C-130
PU mobile
Aerodyne mobile
CU mobile
NOAA mobile
BAO tower

Figure 5.

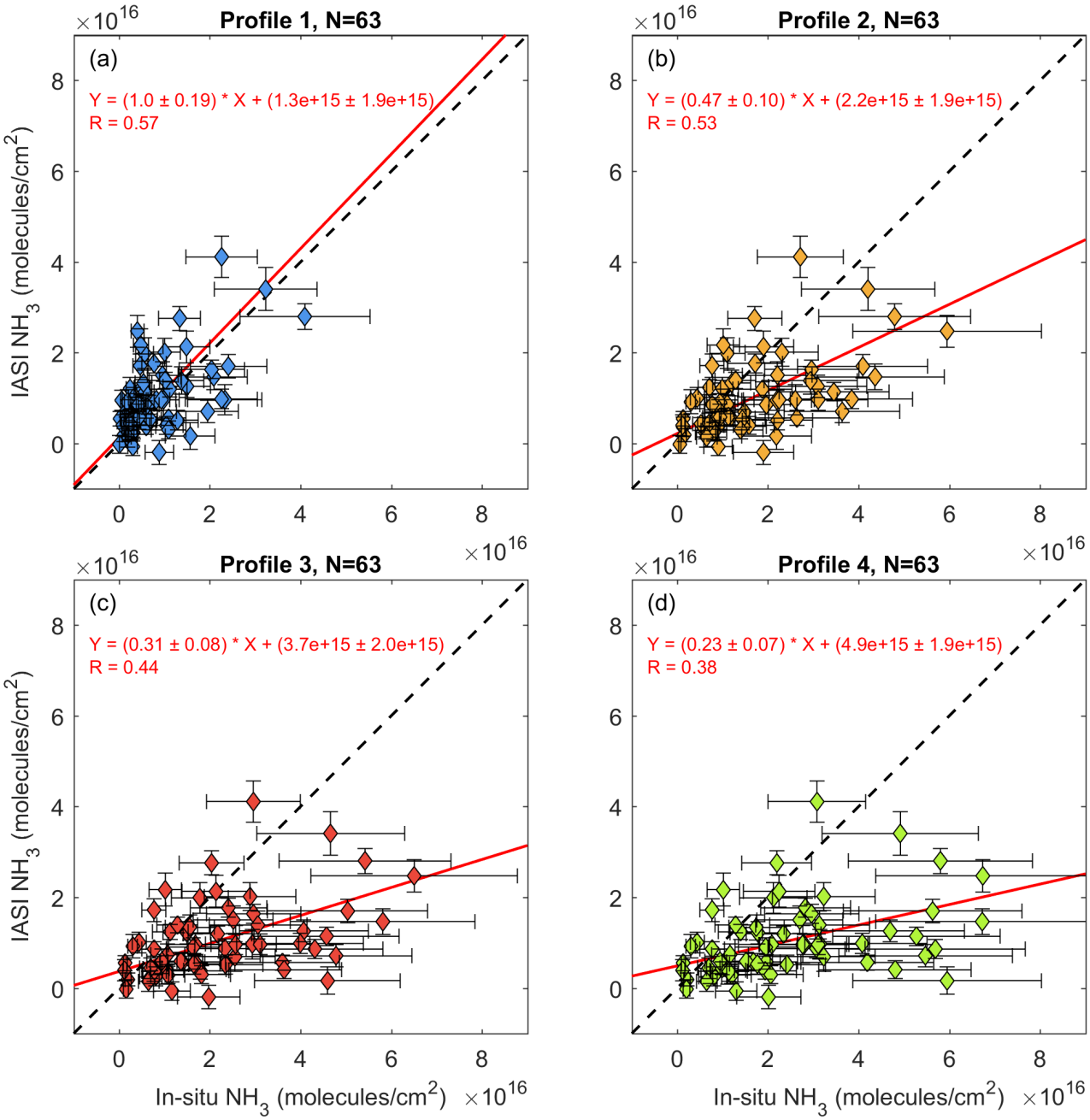
Profile 1, N=63
(a)
Y = (1.0 ± 0.19) * X + (1.3e+15 ± 1.9e+15)
R = 0.57
Profile 2, N=63
(b)
Y = (0.47 ± 0.10) * X + (2.2e+15 ± 1.9e+15)
R = 0.53
Profile 3, N=63
(c)
Y = (0.31 ± 0.08) * X + (3.7e+15 ± 2.0e+15)
R = 0.44
Profile 4, N=63
(d)
Y = (0.23 ± 0.07) * X + (4.9e+15 ± 1.9e+15)
R = 0.38
IASI NH3 (molecules/cm2)
In-situ NH3 (molecules/cm2)
×10^16

Figure 6.

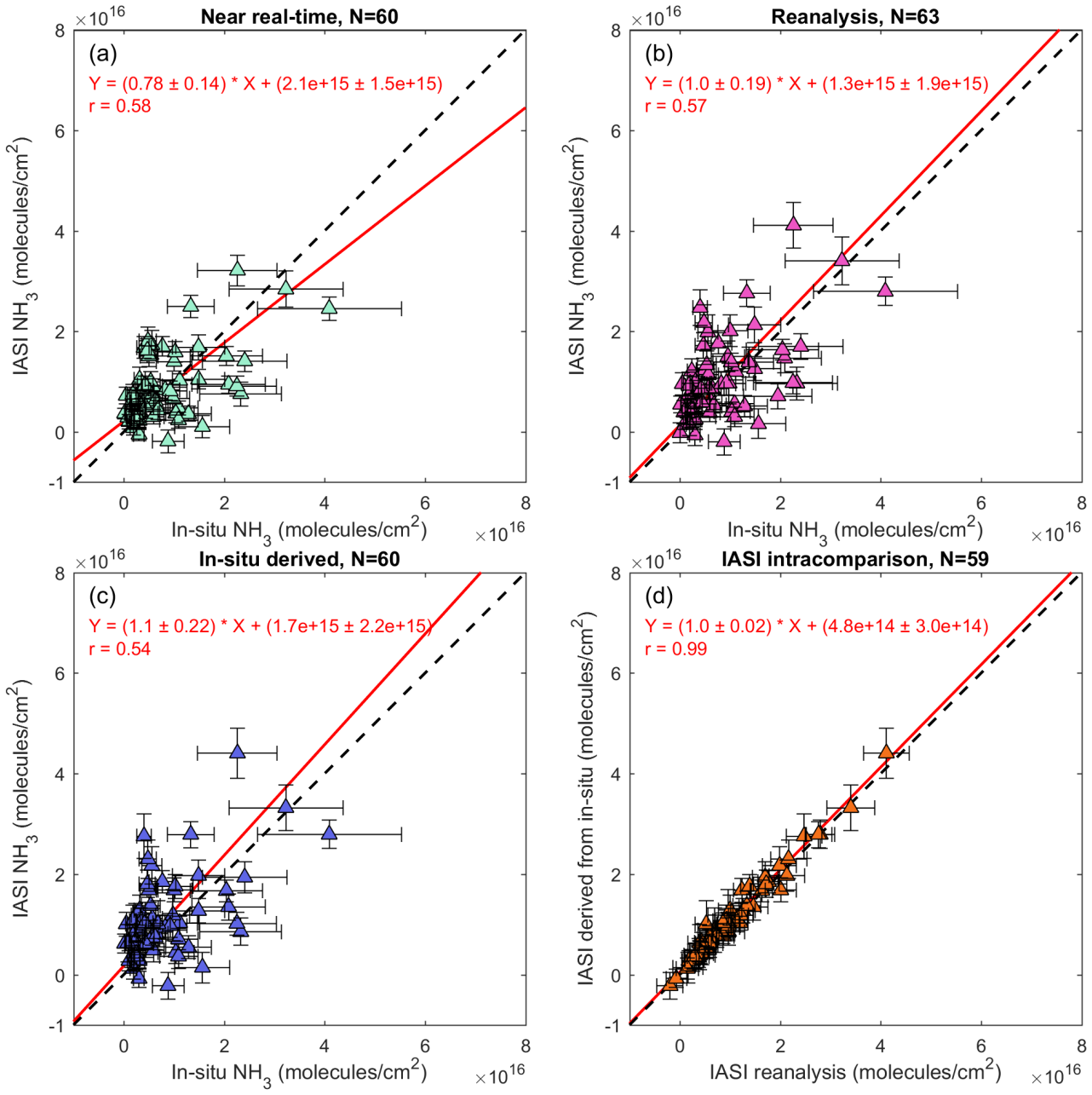
Near real-time, N=60
(a)
Y = (0.78 ± 0.14) * X + (2.1e+15 ± 1.5e+15)
r = 0.58
IASI NH3 (molecules/cm2)
In-situ NH3 (molecules/cm2)
×10^16
Reanalysis, N=63
(b)
Y = (1.0 ± 0.19) * X + (1.3e+15 ± 1.9e+15)
r = 0.57
IASI NH3 (molecules/cm2)
In-situ NH3 (molecules/cm2)
×10^16
In-situ derived, N=60
(c)
Y = (1.1 ± 0.22) * X + (1.7e+15 ± 2.2e+15)
r = 0.54
IASI NH3 (molecules/cm2)
In-situ NH3 (molecules/cm2)
×10^16
IASI intracomparison, N=59
(d)
Y = (1.0 ± 0.02) * X + (4.8e+14 ± 3.0e+14)
r = 0.99
IASI derived from in-situ (molecules/cm2)
IASI reanalysis (molecules/cm2)
×10^16

Figure 7.

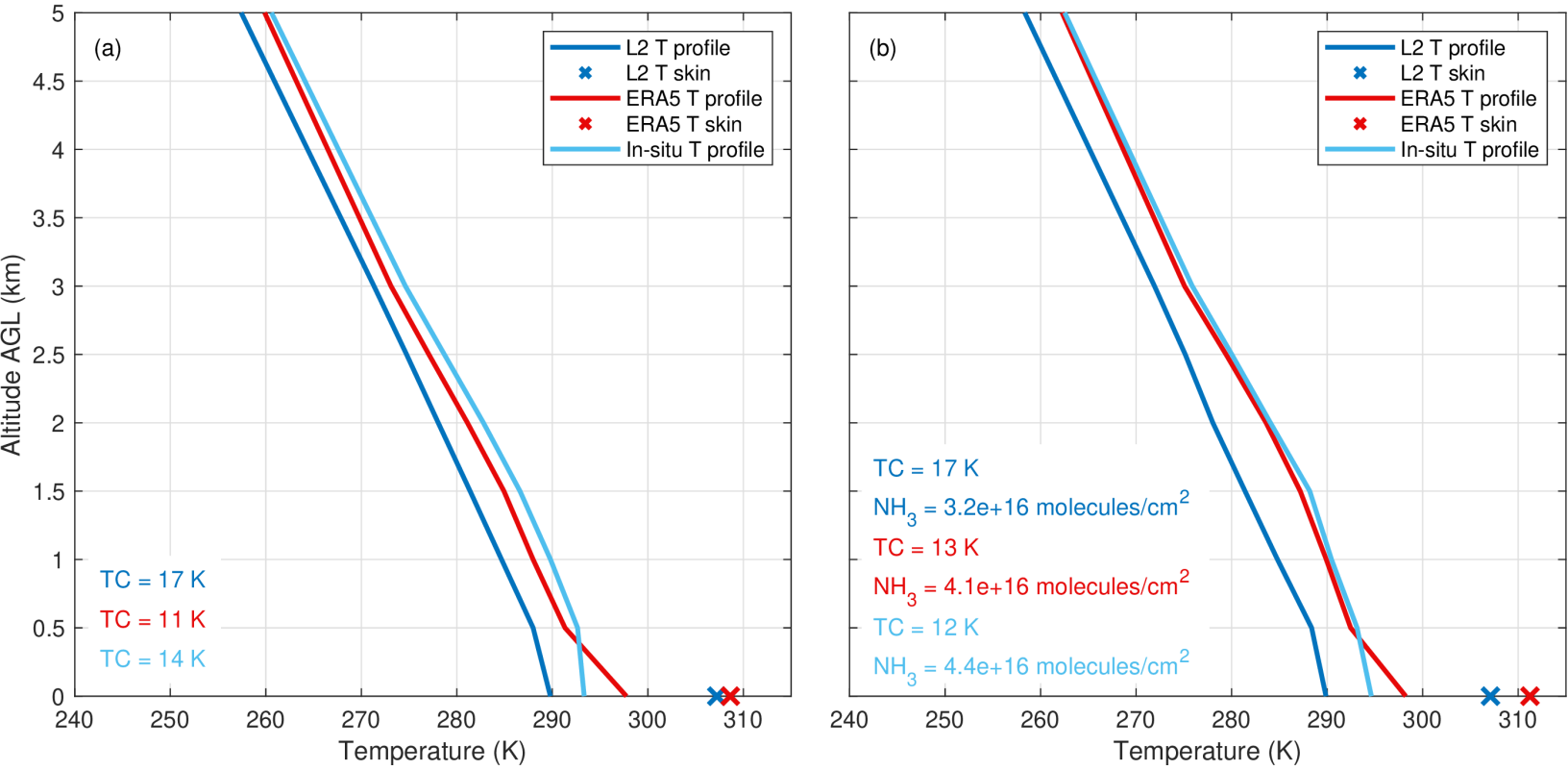
(a)
L2 T profile
L2 T skin
ERA5 T profile
ERA5 T skin
In-situ T profile
TC = 17 K
TC = 11 K
TC = 14 K
Altitude AGL (km)
Temperature (K)
(b)
L2 T profile
L2 T skin
ERA5 T profile
ERA5 T skin
In-situ T profile
TC = 17 K
NH3 = 3.2e+16 molecules/cm2
TC = 13 K
NH3 = 4.1e+16 molecules/cm2
TC = 12 K
NH3 = 4.4e+16 molecules/cm2
Temperature (K)

Figure 8.

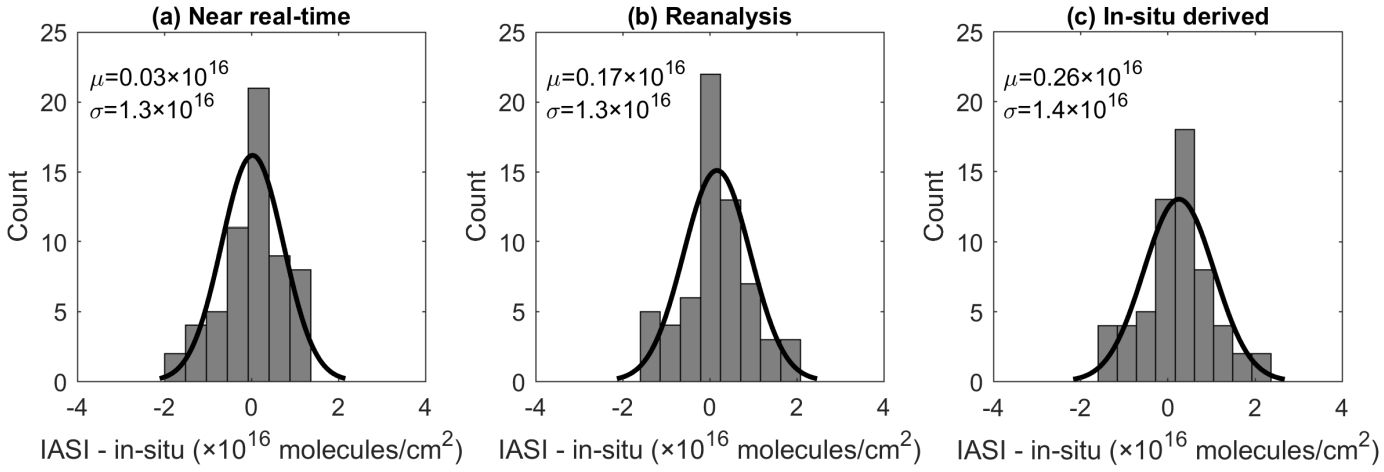
(a) Near real-time
μ=0.03×10^16
σ=1.3×10^16
Count
IASI - in-situ (×10^16 molecules/cm^2)
(b) Reanalysis
μ=0.17×10^16
σ=1.3×10^16
Count
IASI - in-situ (×10^16 molecules/cm^2)
(c) In-situ derived
μ=0.26×10^16
σ=1.4×10^16
Count
IASI - in-situ (×10^16 molecules/cm^2)

Figure 9.

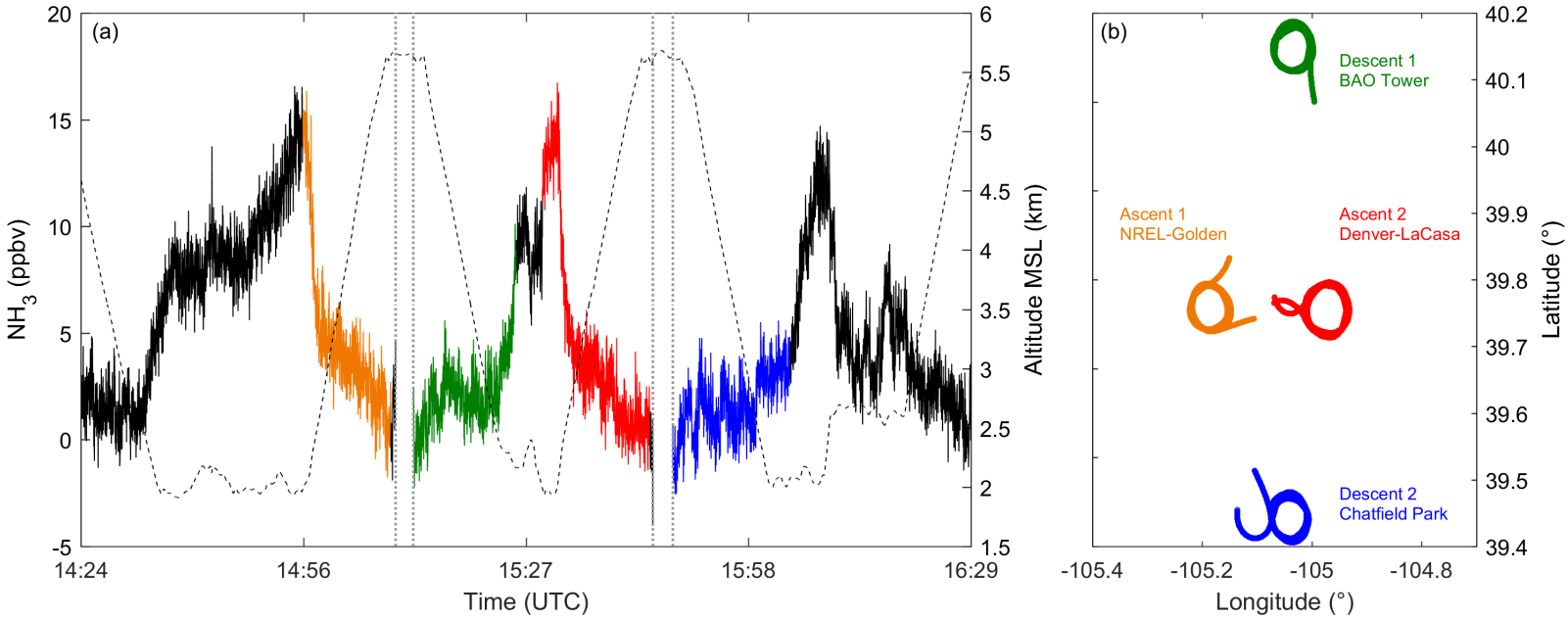
(a)
NH3 (ppbv)
Altitude MSL (km)
Time (UTC)
14:24
14:56
15:27
15:58
16:29
(b)
Descent 1
BAO Tower
Ascent 1
NREL-Golden
Ascent 2
Denver-LaCasa
Descent 2
Chatfield Park
Latitude (°)
Longitude (°)
-105.4
-105.2
-105
-104.8

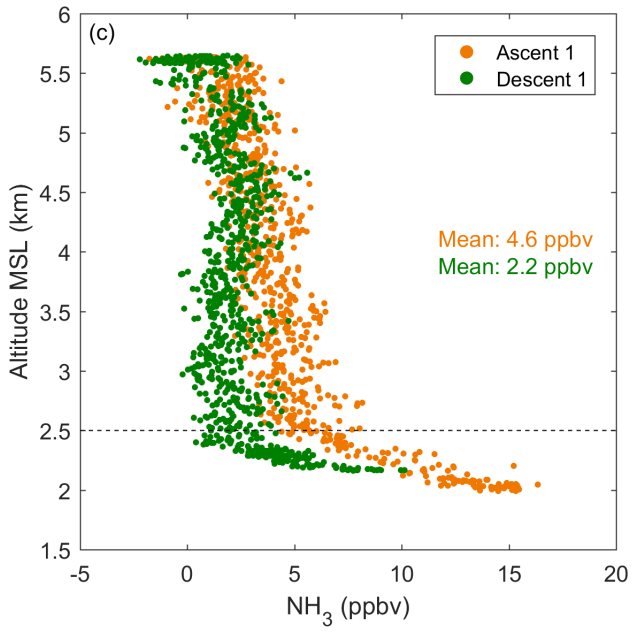
(c)
Ascent 1
Descent 1
Mean: 4.6 ppbv
Mean: 2.2 ppbv
Altitude MSL (km)
NH3 (ppbv)

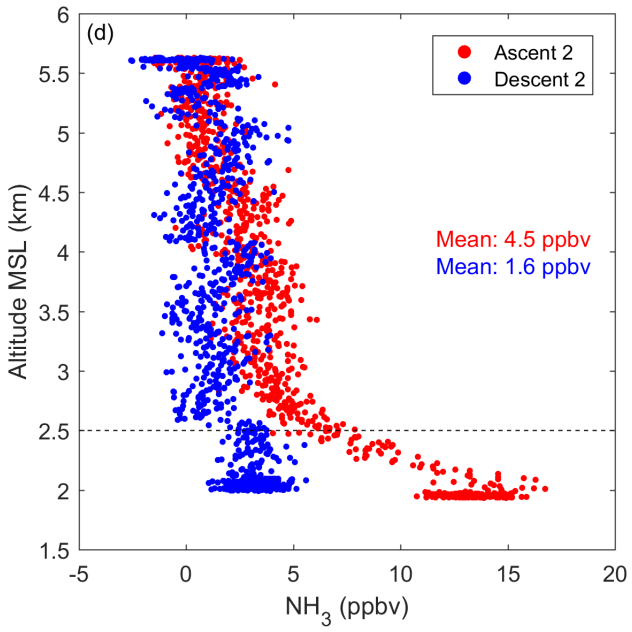
(d)
Ascent 2
Descent 2
Mean: 4.5 ppbv
Mean: 1.6 ppbv
Altitude MSL (km)
NH3 (ppbv)

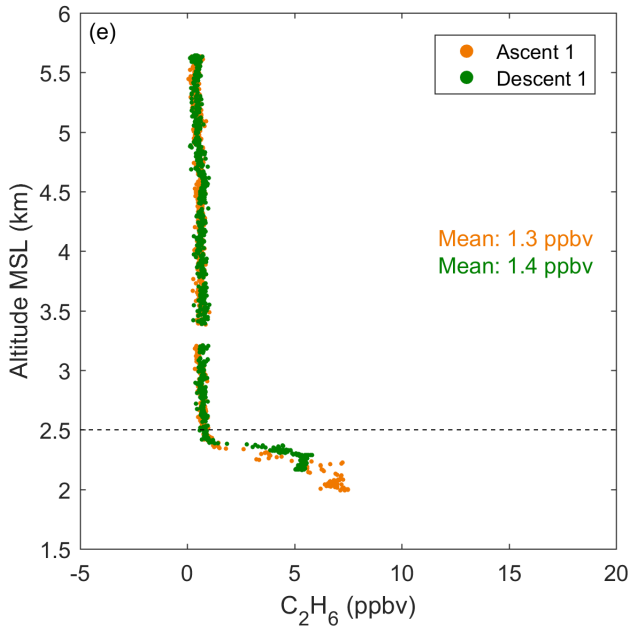
(e)
Ascent 1
Descent 1
Mean: 1.3 ppbv
Mean: 1.4 ppbv
Altitude MSL (km)
C2H6 (ppbv)

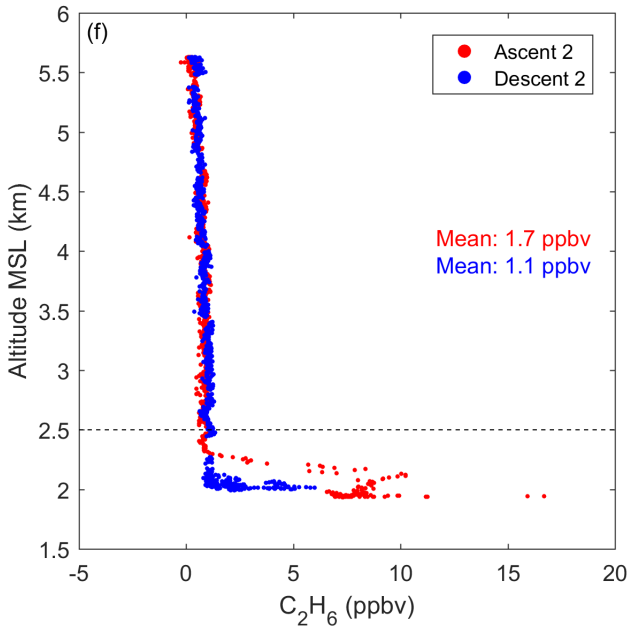
(f)
Ascent 2
Descent 2
Mean: 1.7 ppbv
Mean: 1.1 ppbv
Altitude MSL (km)
C2H6 (ppbv)

Figure 10.

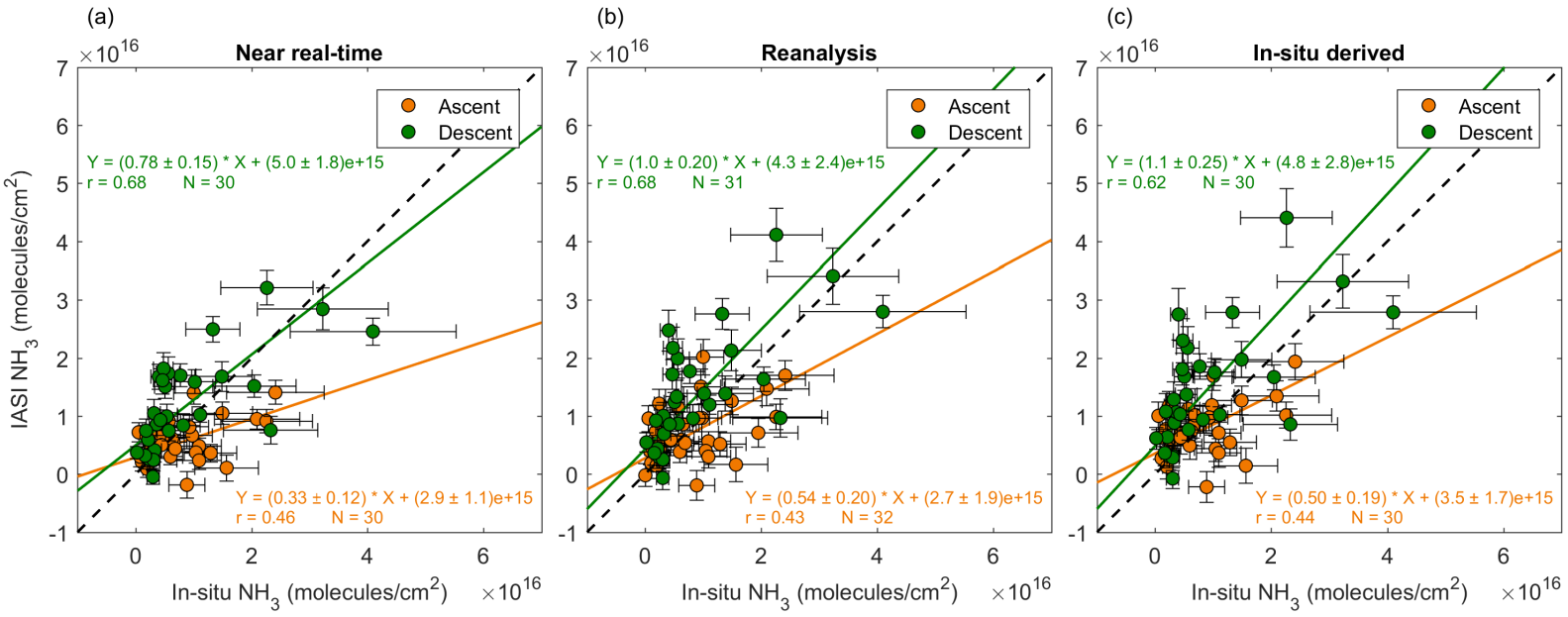
(a)
Near real-time
(b)
Reanalysis
(c)
In-situ derived
Ascent
Descent
Y = (0.78 ± 0.15) * X + (5.0 ± 1.8)e+15
r = 0.68 N = 30
Y = (0.33 ± 0.12) * X + (2.9 ± 1.1)e+15
r = 0.46 N = 30
Y = (1.0 ± 0.20) * X + (4.3 ± 2.4)e+15
r = 0.68 N = 31
Y = (0.54 ± 0.20) * X + (2.7 ± 1.9)e+15
r = 0.43 N = 32
Y = (1.1 ± 0.25) * X + (4.8 ± 2.8)e+15
r = 0.62 N = 30
Y = (0.50 ± 0.19) * X + (3.5 ± 1.7)e+15
r = 0.44 N = 30
IASI NH3 (molecules/cm2)
In-situ NH3 (molecules/cm2)
×10^16

Figure 11.

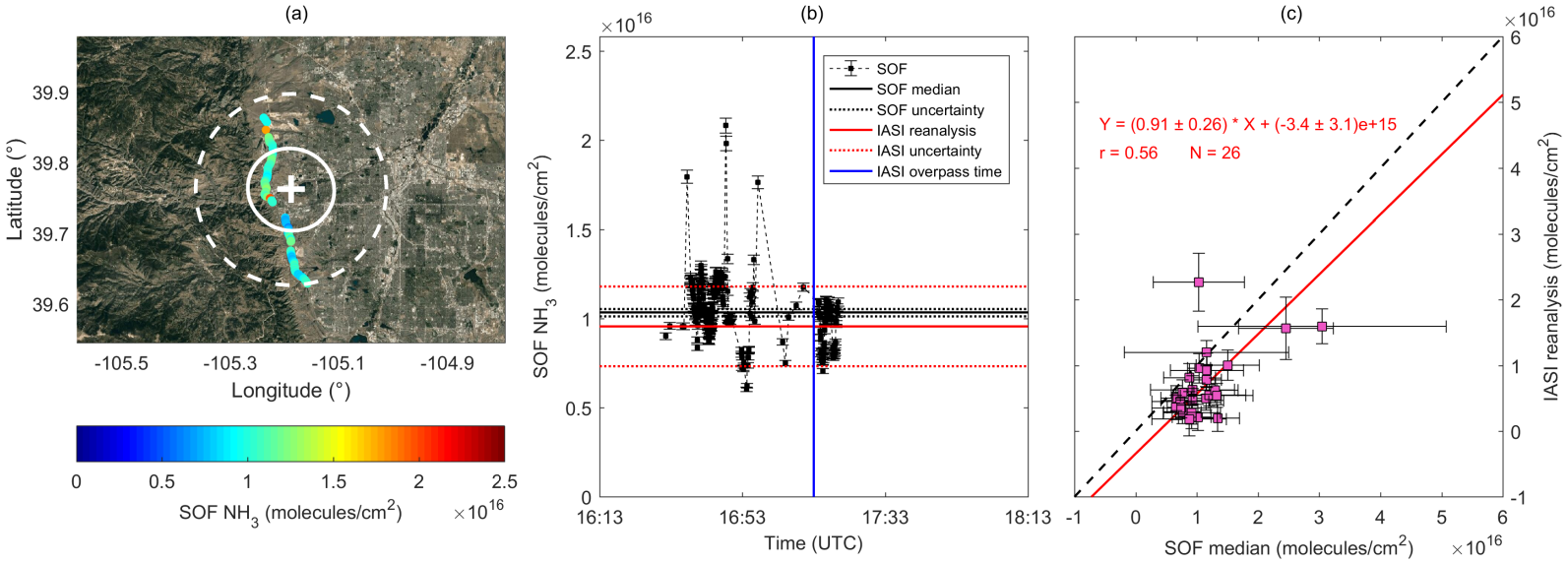
(a)
39.9
39.8
39.7
39.6
Latitude (°)
-105.5
-105.3
-105.1
-104.9
Longitude (°)
0
0.5
1
1.5
2
2.5
SOF NH3 (molecules/cm2)
×10^16
(b)
×10^16
2.5
2
1.5
1
0.5
0
SOF NH3 (molecules/cm2)
SOF
SOF median
SOF uncertainty
IASI reanalysis
IASI uncertainty
IASI overpass time
16:13
16:53
17:33
18:13
Time (UTC)
(c)
×10^16
Y = (0.91 ± 0.26) * X + (-3.4 ± 3.1)e+15
r = 0.56 N = 26
6
5
4
3
2
1
0
-1
IASI reanalysis (molecules/cm2)
-1
0
1
2
3
4
5
6
SOF median (molecules/cm2)
×10^16